



Universiteit
Leiden
The Netherlands

KiDS-1000: cross-correlation with Planck cosmic microwave background lensing and intrinsic alignment removal with self-calibration

Yao, J.; Shan, H.; Zhang, P.; Liu, X.; Heymans, C.; Joachimi, B.; ... ; Yan, Z.

Citation

Yao, J., Shan, H., Zhang, P., Liu, X., Heymans, C., Joachimi, B., ... Yan, Z. (2023). KiDS-1000: cross-correlation with Planck cosmic microwave background lensing and intrinsic alignment removal with self-calibration. *Astronomy & Astrophysics*, 673. doi:10.1051/0004-6361/202346020


Version: Publisher's Version

License: [Creative Commons CC BY 4.0 license](https://creativecommons.org/licenses/by/4.0/)

Downloaded from: <https://hdl.handle.net/1887/3716647>

Note: To cite this publication please use the final published version (if applicable).

KiDS-1000: Cross-correlation with *Planck* cosmic microwave background lensing and intrinsic alignment removal with self-calibration

Ji Yao^{1,2,3} , Huanyuan Shan¹, Pengjie Zhang^{2,3,4}, Xiangkun Liu⁵, Catherine Heymans^{6,7}, Benjamin Joachimi⁸, Marika Asgari⁹, Maciej Bilicki¹⁰, Hendrik Hildebrandt⁶, Konrad Kuijken¹¹, Tilman Tröster⁶, Jan Luca van den Busch^{8,12}, Angus Wright⁷, and Ziang Yan⁷

¹ Shanghai Astronomical Observatory (SHAO), Nandan Road 80, Shanghai 200030, PR China
e-mail: ji.yao@shao.ac.cn; hyshan@shao.ac.cn

² Department of Astronomy, School of Physics and Astronomy, Shanghai Jiao Tong University, Shanghai 200240, PR China
e-mail: zhangpj@sjtu.edu.cn

³ Shanghai Key Laboratory for Particle Physics and Cosmology, Shanghai 200240, PR China

⁴ Tsung-Dao Lee Institute, Shanghai 200240, PR China

⁵ South-Western Institute for Astronomy Research, Yunnan University, Kunming 650500, PR China

⁶ Institute for Astronomy, University of Edinburgh, Royal Observatory, Blackford Hill, Edinburgh EH9 3HJ, UK

⁷ Ruhr-Universität Bochum, Astronomisches Institut, German Centre for Cosmological Lensing (GCCL), Universitätsstr. 150, 44801 Bochum, Germany

⁸ Department of Physics and Astronomy, University College London, Gower Street, London WC1E 6BT, UK

⁹ E.A Milne Centre, University of Hull, Cottingham Road, Hull HU6 7RX, UK

¹⁰ Center for Theoretical Physics, Polish Academy of Sciences, al. Lotników 32/46, 02-668 Warsaw, Poland

¹¹ Leiden Observatory, Leiden University, PO Box 9513, 2300 RA Leiden, The Netherlands

¹² Argelander-Institut für Astronomie, Universität Bonn, Auf dem Hügel 71, 53121 Bonn, Germany

Received 30 January 2023 / Accepted 14 March 2023

ABSTRACT

Context. Galaxy shear and cosmic microwave background (CMB) lensing convergence cross-correlations contain additional information on cosmology with respect to auto-correlations. While remaining immune to certain systemic effects, these cross-correlations are nonetheless affected by the galaxy’s intrinsic alignments (IA). These effects may, in fact, be responsible for the reported low lensing amplitude of the galaxy shear \times CMB convergence cross-correlations, compared to the standard *Planck* Λ CDM (cosmological constant and cold dark matter) cosmology predictions.

Aims. In this work, we investigate how IA affects the Kilo-Degree Survey (KiDS) galaxy lensing shear and *Planck* CMB lensing convergence cross-correlation and we compare it to previous treatments, both with and without IA taken into consideration.

Methods. We compared the marginalization over IA parameters and the IA self-calibration (SC) method (with additional observables defined only from the source galaxies) to demonstrate that SC can efficiently break the degeneracy between the CMB lensing amplitude, A_{lens} , and the IA amplitude, A_{IA} . We further investigated how different systematics affect the resulting A_{IA} and A_{lens} and we validated our results with the MICE2 simulation.

Results. We find that by including the SC method to constrain IA, the information loss due to the degeneracy between CMB lensing and IA is strongly reduced. The best-fit values are $A_{\text{lens}} = 0.84^{+0.22}_{-0.22}$ and $A_{\text{IA}} = 0.60^{+1.03}_{-1.03}$, while different angular scale cuts can affect A_{lens} by $\sim 10\%$. We show that an appropriate treatment of the boost factor, cosmic magnification, and photometric redshift modeling is important for obtaining the correct IA and cosmological results.

Key words. large-scale structure of Universe – galaxies: formation – gravitational lensing: weak

1. Introduction

Weak lensing due to the distortion of light by gravity is a powerful probe of the underlying matter distribution and the encoded information on cosmological physics such as dark matter, dark energy, and the nature of gravity (Refregier 2003; Mandelbaum 2018). The auto-correlation statistics have been widely used in such analyses, both for galaxy lensing shear, for instance, “cosmic shear” (Hildebrandt et al. 2017; Hikage et al. 2019; Hamana et al. 2020; Asgari et al. 2021; Secco et al. 2022; Amon et al. 2022), as well as cosmic microwave background (CMB) lensing convergence (Planck Collaboration VIII 2020; Omori et al. 2017). Furthermore, cross-correlations between

galaxy shear and CMB lensing have been measured extensively (Hand et al. 2015; Chisari et al. 2015; Liu & Hill 2015; Kirk et al. 2016; Harnois-Déraps et al. 2016, 2017; Singh et al. 2017a; Omori et al. 2019; Namikawa et al. 2019; Marques et al. 2020; Robertson et al. 2021). Cross-correlation statistics contain highly complementary information with respect to auto-correlations, both for cosmology and the cross-checking of systematics. They partly reveal the hidden redshift information in CMB lensing and are more sensitive to structure growth at redshifts between the epochs probed by galaxy shear and CMB lensing. Cross-correlations are also immune to additive errors in shear measurement and provide an external diagnosis of multiplicative errors (Schaan et al. 2017).

Most existing cross-correlation measurements have found a lower CMB lensing amplitude than the prediction of their assumed Λ CDM cosmology (Hand et al. 2015; Liu & Hill 2015; Kirk et al. 2016; Harnois-Déraps et al. 2016, 2017; Singh et al. 2017a; Marques et al. 2020; Robertson et al. 2021). This ratio is normally referred as the CMB lensing amplitude, $A_{\text{lens}} \sim 0.5\text{--}0.9$, although the deviation from unity is only within $1\text{--}2\sigma$. The low lensing amplitude is consistent across many combinations of data sets and analytical methods, suggesting the existence of a common systematic errors or a deviation from the best-fit *Planck* cosmology. This might be related to the tension between galaxy lensing surveys and *Planck* CMB observations (Lin & Ishak 2017; Chang et al. 2019; Heymans et al. 2021) with *Planck*'s internal inconsistencies (Planck Collaboration I 2020; Planck Collaboration VI 2020). In this paper, we focus on the galaxy intrinsic alignment (IA), which can mimic weak lensing signals (Croft & Metzler 2000; Catelan et al. 2001; Crittenden et al. 2001; Lee & Pen 2002; Jing 2002; Hirata & Seljak 2004; Heymans et al. 2004; Bridle & King 2007; Okumura et al. 2009; Joachimi et al. 2013; Kiessling et al. 2015; Blazek et al. 2015, 2019; Rong et al. 2015; Krause et al. 2016; Chisari et al. 2017; Xia et al. 2017; Troxel et al. 2018; Samuroff et al. 2019, 2021; Yao et al. 2020a,b). Here, the CMB lensing convergence is expected to be anticorrelated with respect to the intrinsic ellipticities of the foreground galaxy field, resulting in a dilution of the overall cross-correlation signal (Troxel & Ishak 2014; Chisari et al. 2015; Kirk et al. 2015; Omori et al. 2019; Robertson et al. 2021). Taking IA into account can alleviate the tension in A_{lens} , at the expense of a significant loss of lensing constraining power because of the degeneracy between the lensing amplitude, A_{lens} , and the IA amplitude, A_{IA} . Therefore, a common compromise is to fix both the IA model and its amplitude A_{IA} (Kirk et al. 2016; Harnois-Déraps et al. 2017; Omori et al. 2019) or to assume a strong prior (Robertson et al. 2021).

Since IA is already a major limiting factor in the current cross-correlation analysis, its mitigation will be essential for upcoming measurements with significantly smaller statistical errors. We utilize the IA self-calibration (SC) method (Zhang 2010a,b; Troxel & Ishak 2012b,a; Yao et al. 2017, 2019), a galaxy-galaxy lensing method that is based on a different weighting scheme, to mitigate the IA problem in the shear-convergence cross-correlation. It draws on the fact that the IA-galaxy correlation is insensitive to the redshift order, while it does indeed matter for lensing-galaxy correlations whether the lens is in front of the source or not. Therefore, we can isolate IA by comparing extra observables, namely, the galaxy shear \times number density cross-correlation with a different weighting of the redshift pairs. This measurement of IA is independent of a physical model of the IA and requires no data external to the shear data. SC was first applied to KiDS450/KV450 (Yao et al. 2020a; Pedersen et al. 2020) and DECaLS DR3 (Yao et al. 2020b) and has enabled significant IA detections. The detected IA signal can then be applied to remove IA in the lensing shear auto-correlation and shear-convergence cross-correlation. The IA information is obtained from a shear \times number density cross-correlation within the same photometric redshift (photo- z) bin and (more importantly) with different weighting schemes on the photo- z ordering, which is usually not used for cosmological parameter constraints. We find that this removal of IA leads no almost no losses in terms of cosmological information.

In a previous work Yao et al. (2020b), we demonstrated the importance and methodology of including certain types of systematics in the SC lensing-IA separation method, namely, galaxy

bias, covariance between the separated lensing signal and IA signal, IA signal drop Q^{lg} due to the photo- z selection, and scale dependency among the signal drops, Q^{Gg} and Q^{lg} . In this work, we further investigate other sources of systematics, including the boost factor (Mandelbaum et al. 2005), photo- z modeling bias (Yao et al. 2020a), and cosmic magnification (Bartelmann 1995; Bartelmann & Schneider 2001; Yang et al. 2017; Liu et al. 2021). Interestingly, as the survey goes to higher redshift, the contamination to the SC method from magnification quickly increases to a non-negligible level. The cosmic magnification will change the observed galaxy number density due to the lensing-magnified flux and lensing-enlarged area, thereby biasing our SC analysis. We investigate the proper treatments for the above systematics together with the cosmological study.

This paper is organized as follows. In Sect. 2, we review the physics of galaxy shear \times CMB convergence and how our SC method works to subtract the IA information. In Sect. 3, we introduce the KiDS-1000 and *Planck* data used in this work, and the MICE2 simulation (Fosalba et al. 2015; van den Busch et al. 2020) we use to validate how the SC method is affected by different systematics. We show the measurements of the observables in Sect. 4. The results and summary are shown in Sects. 5 and 6.

2. Methods

We applied our self-calibration method to separate the intrinsic alignment and the lensing signals and show how the intrinsic alignment will bias the galaxy shear-CMB convergence correlation. In this section, we review the theory of lensing cross-correlation and the self-calibration method, with a modification to account for the contamination from cosmic magnification.

2.1. Galaxy shear \times CMB convergence

The gravitational field can distort the shape of the background source galaxy image and introduce an extra shape that is tangentially aligned to the lens. This gravitational shear γ^{G} of the source galaxy contains integral information of the foreground overdensity along the line of sight (Bartelmann & Schneider 2001). Similarly, the photons from the CMB are deflected, and the lensing convergence, κ , can be reconstructed from the CMB temperature and polarization observations (Planck Collaboration VIII 2020). By correlating these two quantities ($\gamma^{\text{G}}\kappa$), we probe the clustering of the underlying matter field $\langle\delta\delta\rangle$. In harmonic space, while assuming flat space (Omori et al. 2019; Marques et al. 2020), we have:

$$C^{\kappa^{\text{gal}}\kappa^{\text{CMB}}}(\ell) = \int_0^{\chi^{\text{CMB}}} \frac{q^{\text{gal}}(\chi)q^{\text{CMB}}(\chi)}{\chi^2} P_{\delta}\left(k = \frac{\ell + 1/2}{\chi}, z\right) d\chi. \quad (1)$$

Equation (1) is the galaxy-lensing CMB-lensing cross-angular power spectrum, which probes the matter power spectrum, $P_{\delta}(k, z)$, as well as the background geometry, $\chi(z)$, when precision allows. Here, z is the redshift, χ is the comoving distance, k is the wavenumber, ℓ is the angular mode, $q^{\text{gal}}(\chi)$ and $q^{\text{CMB}}(\chi)$ are the lensing efficiency functions for galaxy-lensing and CMB-lensing, with the analytical forms:

$$q^{\text{gal}}(\chi_1) = \frac{3}{2}\Omega_{\text{m}}\frac{H_0^2}{c^2}(1+z_1)\int_{\chi_1}^{\infty} n(\chi_s)\frac{(\chi_s - \chi_1)\chi_1}{\chi_s} d\chi_s, \quad (2)$$

$$q^{\text{CMB}}(\chi_1) = \frac{3}{2}\Omega_{\text{m}}\frac{H_0^2}{c^2}(1+z_1)\frac{(\chi_s - \chi_1)\chi_1}{\chi_s}, \quad (3)$$

where χ_s and χ_l are the comoving distance to the source and lens, and χ_s in Eq. (3) takes CMB as the source of light ($z \sim 1100$). We note the spacial curvature $\Omega_k = 0$ is assumed so that the comoving angular diameter distances in Eqs. (2) and (3) are replaced with the comoving radial distances. Here, $n(\chi)$ gives the source galaxy distribution as a function of comoving distance and it is connected with the galaxy redshift distribution via $n(\chi) = n(z)dz/d\chi$. In this work, we only use one redshift bin due to the limit of the total S/N on the CMB lensing signal, while a tomographic example can be found in Harnois-Déraps et al. (2017). In the future, with higher S/N (e.g., for CMB-S4¹ × LSST²), tomography can be used to subtract more cosmological information.

The shear-convergence cross-correlation function measured in real space is given by the Hankel transformation:

$$w^{G\kappa}(\theta) = \frac{1}{2\pi} \int_0^\infty d\ell \ell C^{\kappa^{\text{gal}}\kappa^{\text{CMB}}}(\ell) J_2(\ell\theta), \quad (4)$$

where $J_2(x)$ is the Bessel function of the first kind and order 2. Here, “G” represents the gravitational lensing shear, γ^G , that is to be separated from the intrinsic alignment, γ^I , in the following section.

In addition, due to the current low S/N, we chose not to investigate the full cosmological constraints in this work. Instead, we performed a matched-filter fitting, with a lensing amplitude, A_{lens} , that suits $\hat{w}^{G\kappa} = A_{\text{lens}} w^{G\kappa}$, where $\hat{w}^{G\kappa}$ is the measured correlation function and $w^{G\kappa}$ is the theoretical model.

2.2. Intrinsic alignment of galaxies

The observed galaxy shear estimator contains three components: gravitational shear, an intrinsic alignment term, and random noise, namely, $\hat{\gamma} = \gamma^G + \gamma^I + \gamma^N$. Both the gravitational shear and the IA term are related to the underlying matter overdensity δ and are associated with the large-scale structure. This means that when we cross-correlate the galaxy shape and the CMB convergence, there will be contributions from both lensing and IA:

$$\langle \hat{\gamma}\kappa \rangle = \langle \gamma^G\kappa \rangle + \langle \gamma^I\kappa \rangle. \quad (5)$$

Therefore, the IA part of the correlation will contaminate the measurement and lead to a bias in the lensing amplitude, A_{lens} , or the cosmological parameters when assuming $\langle \hat{\gamma}\kappa \rangle = \langle \gamma^G\kappa \rangle$.

The IA-convergence correlation function is linked to the IA-convergence power spectrum:

$$C^{I\kappa^{\text{CMB}}} = \int_0^{\chi_{\text{CMB}}} \frac{n(\chi)q^{\text{CMB}}(\chi)}{\chi^2} P_{\delta,\gamma^I} \left(k = \frac{\ell + 1/2}{\chi}, z \right) d\chi. \quad (6)$$

Here, P_{δ,γ^I} is the 3D matter-IA power spectrum. The conventional method is to assume an IA model with some nuisance parameters, which will enter the fitting process. The most widely used IA model is the non-linear linear tidal alignment model (Catelan et al. 2001; Hirata & Seljak 2004; Bridle & King 2007), expressed as:

$$P_{\delta,\gamma^I} = -A_{\text{IA}}(L, z) \frac{C_1 \rho_{m,0}}{D(z)} P_\delta(k; \chi), \quad (7)$$

which is proportional to the non-linear matter power spectrum P_δ , suggesting that the IA is caused by the gravitational tidal field. Then, A_{IA} is the IA amplitude, which can be

¹ <https://cmb-s4.org/>

² Legacy Survey of Space and Time, Vera C. Rubin Observatory, <https://www.lsst.org/>

redshift(z)- and luminosity(L)-dependent (Joachimi et al. 2011). Its redshift evolution has been measured recently in simulations (Chisari et al. 2016; Samuroff et al. 2021) and in observations with low significance (Johnston et al. 2019; Yao et al. 2020b; Secco et al. 2022; Tonegawa & Okumura 2022). The other related quantities include: the mean matter density of the universe at $z = 0$, expressed as $\rho_{m,0} = \rho_{\text{crit}}\Omega_{m,0}$; $C_1 = 5 \times 10^{-14} (h^2 M_{\text{sun}}/\text{Mpc}^{-3})$ the empirical amplitude taken from Brown et al. (2002) and the normalized linear growth factor $D(z)$. We note that the IA model in Eq. (7) can be replaced by more complicated models as in Krause et al. (2016), Blazek et al. (2015, 2019), Fortuna et al. (2021) for different samples (Yao et al. 2020b; Zjupa et al. 2020; Samuroff et al. 2021). The self-calibration method can introduce new observables to constrain IA with additional constraining power, and in the future when the signal-to-noise (S/N) allows, it can be extended to constrain more complicated IA models.

2.3. Self-calibration of intrinsic alignment

The IA self-calibration (SC) method (Zhang 2010b; Yao et al. 2017, 2019, 2020a,b) uses the same galaxy sample as both the source and the lens, which is different from most galaxy-galaxy lensing studies. It introduces two observables: the shape-galaxy correlation in the same redshift bin, w^{γ^g} , and a similar correlation, $w^{\gamma^g}|_s$, using the pairs where the photo- z of the source galaxy is lower than the photo- z of the lens galaxy, namely:

$$z_{\gamma^g}^P < z_g^P, \quad (8)$$

which is denoted in this work as “the SC selection”.

In this work, we extend our methodology to include the impact from cosmic magnification (Bartelmann 1995; Bartelmann & Schneider 2001; Yang et al. 2017; Liu et al. 2021). Because of the existence of magnification, the intrinsic galaxy number density field, δ_g , is affected by the foreground lensing convergence, κ^{gal} , leading to a lensed galaxy overdensity:

$$\delta_g^L = \delta_g + g_{\text{mag}}\kappa^{\text{gal}}, \quad (9)$$

where the prefactor writes $g_{\text{mag}} = 2(\alpha - 1)$ for a complete and flux-limited sample. It accounts for the increase in galaxy number density due to lensing-magnified flux ($\alpha = -d \ln N/d \ln F$, where $N(F)$ denotes the galaxy number N that is brighter than the flux limit F) and the decrease of galaxy number density due to the lensing-area-enlargement (-2 in g_{mag}). The observed shape-galaxy correlation is given by:

$$\langle \hat{\gamma}\delta_g^L \rangle = \langle (\gamma^G + \gamma^I)(\delta_g + g_{\text{mag}}\kappa^{\text{gal}}) \rangle. \quad (10)$$

The two SC observables can be written as:

$$w_{ii}^{\gamma^g L}(\theta) = w_{ii}^{\text{Gg}}(\theta) + w_{ii}^{\text{Ig}}(\theta) + g_{\text{mag}} \left[w_{ii}^{\text{Gg}^{\text{gal}}}(\theta) + w_{ii}^{\text{Ig}^{\text{gal}}}(\theta) \right], \quad (11)$$

$$w_{ii}^{\gamma^g L}|_s(\theta) = w_{ii}^{\text{Gg}}|_s(\theta) + w_{ii}^{\text{Ig}}|_s(\theta) + g_{\text{mag}} \left[w_{ii}^{\text{Gg}^{\text{gal}}}|_s(\theta) + w_{ii}^{\text{Ig}^{\text{gal}}}|_s(\theta) \right], \quad (12)$$

where “|_s” denotes the SC selection, and i denotes the i -th redshift bin if tomography is applied. The lensing-galaxy w^{Gg} and the IA-galaxy w^{Ig} signal are affected by this SC selection, as quantified by the Q parameters:

$$Q_i^{\text{Gg}}(\theta) \equiv \frac{w_{ii}^{\text{Gg}}|_s(\theta)}{w_{ii}^{\text{Gg}}(\theta)}, \quad (13)$$

$$Q_i^{\text{Ig}}(\theta) \equiv \frac{w_{ii}^{\text{Ig}}|_s(\theta)}{w_{ii}^{\text{Ig}}(\theta)}. \quad (14)$$

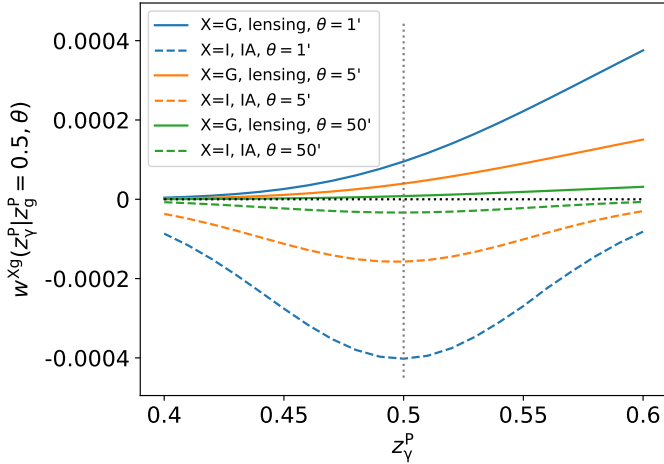


Fig. 1. Toy model to illustrate the different redshift dependences for the lensing signal and the IA signal and to explain why the SC selection Eq. (8) works. We placed many lens galaxies at photo- z $z_g^P = 0.5$ (the grey dotted line), while allowing the photo- z of the source galaxies z_g^P to change (x -axis) to evaluate the corresponding lensing correlation function w^{Gg} or IA correlation function w^{Ig} at different angular separation θ . The true- z has a Gaussian scatter of 0.04 (this number is chosen for display purposes, so that the lensing/IA signals have comparable maximum and minimum values) around the photo- z , for both source galaxies and lens galaxies. As the gravitational lensing shear is an optical shape that requires $z_g < z_\gamma$, it will have a non-symmetric power around z_g^P , as the positive solid curves show. This also demonstrate $Q^{Gg} \ll 1$ according to Eq. (13). As the IA shape is a dynamical shape, it does not have requirements on the relative redshifts, leading to a symmetric power around z_g^P , as the negative dashed curves show. This also demonstrate $Q^{Ig} \sim 1$ according to Eq. (14). These relations hold for signals at different angular separations (different colors). The different IA models (which could deviate from Eq. (7) and with $A_{IA} = 1$ being assumed) will only change the relative amplitudes of the negative signals at different scales, but not the redshift-dependency around z_g^P . We note that at such a redshift range, the magnification signal is much smaller than the IA signal.

For the lensing signal to exist, the redshift of the source, z_γ , needs to be greater than the redshift of the lens, z_g : $z_\gamma > z_g$. The SC photo- z selection $z_\gamma^P < z_g^P$ largely reduces the lensing signal, leading to $Q^{Gg} \ll 1$. The IA signal does not rely on the ordering along the line of sight, with $Q^{Ig} \sim 1$. The lensing drop, Q^{Gg} , and the IA drop, Q^{Ig} , are dependent on the photo- z quality, as described in Zhang (2010b), Yao et al. (2017, 2020a,b). If the photo- z quality is perfect, the SC selection will result in no lensing signal so that Q^{Gg} approaches 0. For incorrect photo- z s, the SC selection fails and Q^{Gg} is ~ 1 . Given a photo- z distribution $n^P(z^P)$ and the true- z distribution $n(z)$, the lensing-drop Q^{Gg} and IA-drop Q^{Ig} can be theoretically derived, following Yao et al. (2020a,b), with more technical details provided in Appendix A. We also present a toy model to visualize how the SC selection works in Fig. 1.

We quantitatively test the terms in Eq. (11), finding they generally follow $|w^{Ikgal}| < |w^{Gkgal}| \ll |w^{Ig}| < |w^{Gg}|$ for $z < 0.9$ data; therefore, in previous analyses (Zhang 2010b; Yao et al. 2020a,b), the magnification terms were neglected. For the $z \sim 1$ galaxies, however, the magnification term w^{Gkgal} quickly approaches w^{Ig} and becomes a non-negligible source of contamination to the SC method. In Fig. 2, we show a theoretical comparison of the angular power spectra. We can write the SC selection for the magnification term as $w^{Gkgal}|_S = Q^{Gk} w^{Gkgal}$. At the drop of the signal, $Q^{Gk} \sim Q^{Ig} \sim 1$, and given that these are

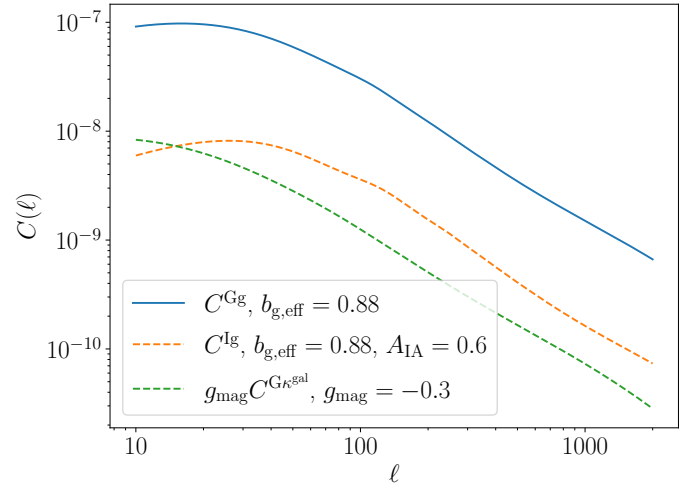


Fig. 2. Theoretical comparison between the galaxy-shear $C^{Gg}(\ell)$, galaxy-IA $C^{Ig}(\ell)$ and shear-magnification $g_{\text{mag}} C^{Gkgal}(\ell)$ angular power spectra, with the best fit of our baseline analysis and the redshift distribution $n(z)$ from KiDS-1000 $0.5 < z^P < 1.2$ shear catalog. The dashed lines represent negative signals. This figure demonstrates that the magnification contamination is important in the self-calibration method for the high- z KiDS source sample.

not z -pair-dependent correlations, the magnification signal w^{Gkgal} will contaminate the IA signal w^{Ig} due to similar behavior, leaving the lensing signal w^{Gg} unaffected. We note the w^{Ik} term is negligible in this work.

After measuring the galaxy-galaxy lensing observables $\{w^{\gamma g^L}, w^{\gamma g^L}|_S\}$ and the drops of the signals, $\{Q^{Gg}, Q^{Ig}\}$, (more details are provided in Eqs. (13) and (14), and Appendix A), the corresponding lensing-galaxy correlation w^{Gg} , IA-galaxy correlation w^{Ig} and shear-magnification correlation w^{Gk} can be linearly obtained:

$$w_{ii}^{Gg}(\theta) = \frac{Q_i^{Ig}(\theta) w_{ii}^{\gamma g^L}(\theta) - w_{ii}^{\gamma g^L}|_S(\theta)}{Q_i^{Ig}(\theta) - Q_i^{Gg}(\theta)}, \quad (15)$$

$$w_{ii}^{Ig}(\theta) + w_{ii}^{Gkgal}(\theta) = \frac{w_{ii}^{\gamma g^L}|_S(\theta) - Q_i^{Gg}(\theta) w_{ii}^{\gamma g^L}(\theta)}{Q_i^{Ig}(\theta) - Q_i^{Gg}(\theta)}. \quad (16)$$

In the previous work, the IA information was directly extracted in w^{Ig} . However, as shown in Fig. 2 and Eq. (16), for KiDS the subtracted signal suffers from the contamination from a magnification term, w^{Gk} . Constraining the measurements of $\{w^{Gg}, w^{Ig} + w^{Gkgal}, w^{\gamma k^{CMB}}\}$ together, including the covariance, will lead to robust constraints on both the lensing amplitude and the nuisance parameters. For the current stage, where the S/N values for the measurements are not very high, we choose to ignore the possible scale-dependent features for the effective galaxy bias $b_{g,\text{eff}}$ and IA amplitude A_{IA} , and assume they are linear and deterministic. The parameters $\{A_{\text{lens}}, A_{IA}, b_{g,\text{eff}}, g_{\text{mag}}\}$ are connected to the observables following:

$$w^{Gg}(\theta) = b_{g,\text{eff}} w_{\text{theory}}^{\text{Gm}}(\theta), \quad (17)$$

$$w^{Ig}(\theta) + w^{Gkgal}(\theta) = b_{g,\text{eff}} A_{IA} w_{\text{theory}}^{\text{Im}}(\theta) + g_{\text{mag}} w_{\text{theory}}^{\text{Gkgal}}(\theta), \quad (18)$$

$$w^{\gamma k^{CMB}}(\theta) = A_{\text{lens}} w_{\text{theory}}^{\text{Gk}^{CMB}}(\theta) + A_{IA} w_{\text{theory}}^{\text{Ik}^{CMB}}(\theta), \quad (19)$$

where “ m ” stands for matter, which is the case if one sets the effective galaxy bias $b_{g,\text{eff}} = 1$. We separate the CMB convergence and the galaxy convergence (due to magnification)

Table 1. Λ CDM cosmological parameters adopted in this work, corresponding to the best-fit cosmology from [Planck Collaboration I \(2020\)](#), and the KiDS-1000 multivariate maximum posterior (MAP) results from the two-point correlation functions ξ_{\pm} , the band powers $C(\ell)$, and the COSEBIs, as in [Asgari et al. \(2021\)](#).

Survey	h_0	$\Omega_b h^2$	$\Omega_c h^2$	n_s	σ_8
<i>Planck</i>	0.673	0.022	0.120	0.966	0.812
KiDS ξ_{\pm}	0.711	0.023	0.088	0.928	0.895
KiDS $C(\ell)$	0.704	0.022	0.132	0.999	0.723
KiDS COSEBI	0.727	0.023	0.105	0.949	0.772

with κ^{CMB} and κ^{gal} . On the LHS of Eqs. (17)–(19), we have the measurements, while on the RHS the correlations $w(\theta)$, we have the theoretical predictions assuming *Planck* cosmology ([Planck Collaboration I 2020](#)), see Table 1. We note the Q values being used to obtain the LHS are also cosmology-dependent, however, the sensitivity is weak as the cosmological part is mostly canceled when taking the ratio in Eqs. (13) and (14). We tested whether the fiducial cosmology is changed to any of the KiDS-1000 cosmologies in Table 1. We see the Q s will change by $\sim 1\%$, similarly to what is found in [Yao et al. \(2020b\)](#), and the resulting changes to the fitting parameters $\{A_{\text{IA}}, b_{\text{g,eff}}, g_{\text{mag}}, A_{\text{lens}}\}$ are negligible. However, considering the RHS, those four fitting parameters are sensitive to the fiducial cosmology used to produce the w_{theory} values when magnification exists, which differs from previous analysis ([Yao et al. 2020b](#)). The theoretical predictions w_{theory} are calculated with CCL³ ([Chisari et al. 2019](#)) and CAMB⁴ ([Lewis et al. 2000](#)). The effective galaxy bias $b_{\text{g,eff}}$ in this work is used to separate from the true galaxy bias of this sample, as we will discuss later it can absorb several sources of systematics.

The theoretical prediction of $w_{\text{theory}}^{\text{G}\kappa^{\text{CMB}}}(\theta)$ is given in Eq. (4), and $w_{\text{theory}}^{\text{I}\kappa^{\text{gal}}}(\theta)$ is obtained similarly with the Hankel transform from its power spectrum as in Eq. (6). The $w_{\text{theory}}^{\text{Gm}}$, $w_{\text{theory}}^{\text{Im}}$, and $w_{\text{theory}}^{\text{G}\kappa^{\text{gal}}}$ terms are the Hankel transform from the following angular power spectra:

$$C^{\text{Gm}}(\ell) = \int_{z_{\text{min}}}^{z_{\text{max}}} \frac{q^{\text{gal}}(\chi)n(\chi)}{\chi^2} P_{\delta} \left(k = \frac{\ell + 1/2}{\chi}, z \right) d\chi, \quad (20)$$

$$C^{\text{Im}}(\ell) = \int_{z_{\text{min}}}^{z_{\text{max}}} \frac{n(\chi)n(\chi)}{\chi^2} P_{\delta,\gamma'} \left(k = \frac{\ell + 1/2}{\chi}, z \right) d\chi, \quad (21)$$

$$C^{\text{G}\kappa^{\text{gal}}}(\ell) = \int_{z_{\text{min}}}^{z_{\text{max}}} \frac{q^{\text{gal}}(\chi)q^{\text{gal}}(\chi)}{\chi^2} P_{\delta} \left(k = \frac{\ell + 1/2}{\chi}, z \right) d\chi. \quad (22)$$

As discussed in previous work ([Yao et al. 2020b](#)), by including the effective galaxy bias, $b_{\text{g,eff}}$, we can obtain an unbiased estimation of A_{IA} . This information will be propagated into Eq. (19) to break the degeneracy between A_{IA} and A_{lens} . In this work, we further extend the fitting to include the impact from magnification with the nuisance parameter, g_{mag} . We show later in this work that an unbiased CMB lensing amplitude, A_{lens} , can be obtained from the simultaneous fitting of Eqs. (17)–(19).

³ Core Cosmology Library, <https://github.com/LSSTDESC/CCL>.

⁴ Code for Anisotropies in the Microwave Background, <https://camb.info/>

3. Data

In this section, we introduce the data we use for the $\langle \gamma \kappa^{\text{CMB}} \rangle$ cross-correlation study. Additionally, we used mock KiDS data, based on the MICE2 simulation (see [van den Busch et al. 2020](#) for details) to quantify the potential bias in the SC method due to magnification, photo- z modeling, and the boost factor.

3.1. KiDS-1000 shear catalog

We used the fourth data release of the Kilo-Degree Survey that covers 1006 deg^2 , known as KiDS-1000 ([Kuijken et al. 2019](#)). It has images from four optical bands, *ugri*, and five near-infrared bands, *ZYJHK_s*. The observed galaxies can reach a primary *r*-band median limiting 5σ point source magnitude at ~ 25 . The shear catalog ([Giblin et al. 2021](#)) contains $\sim 21 \text{ M}$ galaxies and is divided into five tomographic bins in the range $0.1 < z_B < 1.2$ based on the BPZ ([Benítez 2000](#)) algorithm. The ellipticity dispersion σ_{ϵ} is ~ 0.27 per component and the shear multiplicative bias is generally consistent with 0. The KiDS data were processed by THELI ([Erben et al. 2013](#)) and Astro-WISE ([Begeman et al. 2013; de Jong et al. 2015](#)). Shears are measured using lensfit ([Miller et al. 2013](#)), and photometric redshifts are obtained from PSF-matched photometry and calibrated using external overlapping spectroscopic surveys ([Hildebrandt et al. 2021](#)).

The application of SC requires not only an accurate redshift distribution $n(z)$, but also relatively accurate photo- z for each galaxy, serving for the SC selection (Eq. (8)). We previously discussed ([Yao et al. 2020a](#)) the fact that the quality of photo- z is very important for the lensing-IA separation. Therefore in this work, we chose to combine the three high- z bins, namely, bin 3 + 4 + 5 in the KiDS-1000 data, as a large bin so that the photo- z error for an individual galaxy is relatively small compared to the total bin width. The photo- z and the redshift distributions calibrated with self-organizing maps (SOM) are shown in Fig. 3. We chose to use the high- z bins because the CMB lensing efficiency Eq. (3) peaks at $z \sim 1$ to 2 (see lower panel of Fig. 3), while the S/N for the cross-correlation is very low for the two low- z bins of KiDS-1000.

To account for the selection functions for the shape of the footprint ([Mandelbaum et al. 2006](#)) of the overlapped region and the varying galaxy number density due to observations ([Rezaie et al. 2020; Johnston et al. 2021](#)), we divided the region into 200 sub-regions with a resolution of HEALPIX $N_{\text{side}} = 512$ ($\sim 50 \text{ arcmin}^2$ per pixel) and generated random points with 20 times the number of galaxies of the KiDS-1000 shear catalog in each sub-region. The pixels within the same sub-region are assigned the same galaxy numbers. This random catalog is used for the SC-related galaxy-galaxy lensing calculation, while its potential defects will not extend to cross-correlations.

3.2. Planck legacy lensing map

We use the CMB lensing map $\kappa(\theta)$ from the *Planck* data release ([Planck Collaboration VIII 2020](#)). The CMB lensing map is reconstructed with the quadratic estimator with the minimum-variance method combining the temperature map and the polarization map, after foreground removal with the SMICA method ([Planck Collaboration I 2020](#)). It covers $f_{\text{sky}} = 0.671$ of the whole sky with the maximum multiple $\ell = 4096$.

In this work, we combine the footprint from the *Planck* lensing map and the mask of the KiDS-1000 shear catalog, leading to an overlapped region of $\sim 829 \text{ deg}^2$. We include the *Planck*

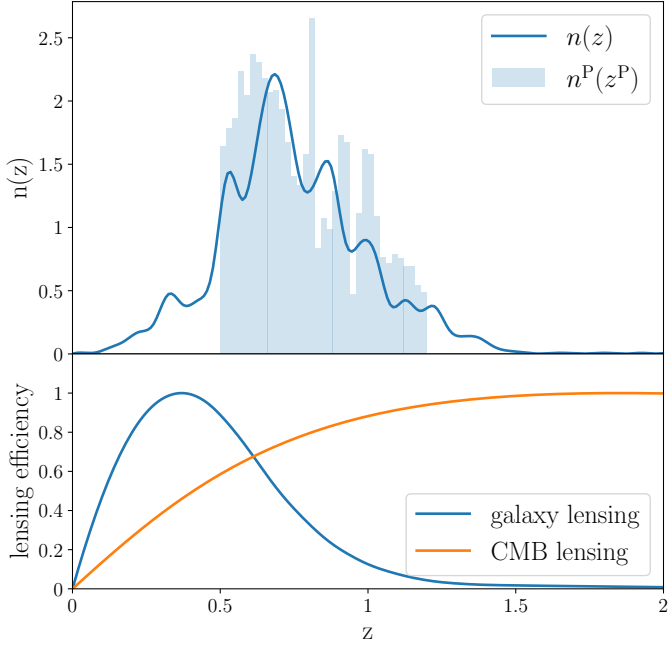


Fig. 3. Photo- z distribution and the reconstructed redshift distribution of the combined galaxy sample in this work from self-organizing maps (SOM). The corresponding galaxy lensing efficiency Eq. (2) and its comparison with CMB lensing efficiency Eq. (3) are shown in the lower panel, with the peak value normalized to 1.

Wiener filter (Planck Collaboration VIII 2020):

$$\hat{\kappa}_{\ell m}^{\text{WF}} = \frac{C_{\ell}^{\phi\phi, \text{fid}}}{C_{\ell}^{\phi\phi, \text{fid}} + N_{\ell}^{\phi\phi}} \hat{\kappa}_{\ell m}^{\text{MV}}, \quad (23)$$

to strengthen the CMB lensing signal at large scales, which will also lead to a suppression of the power spectrum at small scales, where the noise dominates (Dong et al. 2021). The Wiener filter is used both in the CMB lensing κ map and in the theoretical predictions of Eq. (1) to prevent potential bias. After the application of the Wiener filter, we use HEALPY⁵ (Górski et al. 2005; Zonca et al. 2019) to convert the $\kappa_{\ell m}$ to the desired κ -map, and rotate from the galactic coordinates of *Planck* to the J2000 coordinates of KiDS with ASTROPY (Astropy Collaboration 2013). The two-point correlation functions are calculated with TREECORR⁶ (Jarvis et al. 2004).

3.3. MICE2 mock catalog

Additionally, we used the MICE2 simulation gold samples (Fosalba et al. 2015; van den Busch et al. 2020), which highly mimic the KiDS-1000 shear catalog galaxies, to validate our SC method, concerning cosmic magnification and photo- z PDF model bias. MICE2 uses a simulation box width of $3.1 h^{-1} \text{Gpc}$, particle mass resolution of $2.9 \times 10^{10} h^{-1} M_{\odot}$, and a total particle number of $\sim 6.9 \times 10^{10}$. The fiducial cosmology is flat ΛCDM with $\Omega_{\text{m}} = 0.25$, $\sigma_8 = 0.8$, $\Omega_{\text{b}} = 0.044$, $\Omega_{\Lambda} = 0.75$, and $h = 0.7$. The halos were identified with a friends-of-friends algorithm, as in Croce et al. (2015). The galaxies are populated within the halos with a mixture of halo abundance matching (HAM) and halo occupation distribution (HOD) up to $z \sim 1.4$ (Carretero et al. 2015).

⁵ <https://github.com/healpy/healpy>

⁶ <https://github.com/rmjarvis/TreeCorr>

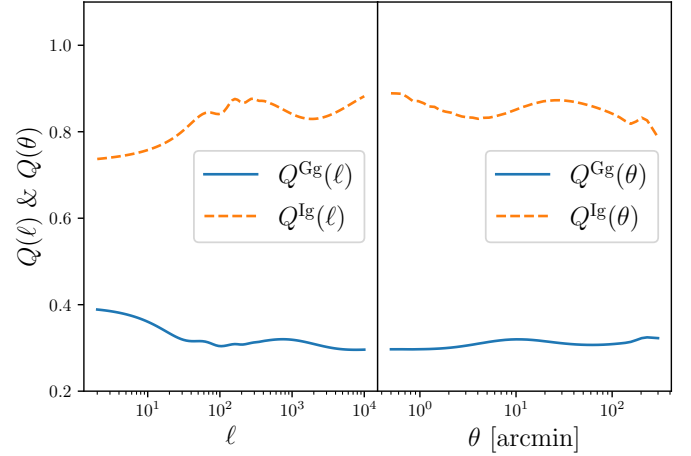


Fig. 4. Lensing-drop Q^{Gg} and the IA-drop Q^{Ig} as a function of ℓ and θ by applying the SC selection Eq. (8); see also Eqs. (13) and (14). These values are adopted to obtain the separation of w^{Gg} and $w^{\text{Ig}} + w^{\text{Gg}^{\text{Gal}}}$, following Eqs. (15) and (16). The left panel shows the calculation from power spectra and the right panel from correlation functions. The right panel is used to transfer $\{w^{\gamma\text{g}}, w^{\gamma\text{g}}|_{\text{S}}\}$ to $\{w^{\text{Gg}}, w^{\text{Ig}}\}$ later in Fig. 6.

We note that in the MICE2 simulation that we use for the KiDS samples, intrinsic alignment is not yet included in the galaxy shapes (while an IA-included version can be found recently in Hoffmann et al. (2022), but for DES⁷, LOWZ (Singh & Mandelbaum 2016), COSMOS⁸, and other possible extensions). The fact that we aim to get $A_{\text{IA}} = 0$ to validate the SC method, while considering systematics from cosmic magnification and photo- z model bias, in addition to what has been addressed in Yao et al. (2020b). We used the galaxy positions (ra, dec), the two noiseless shear components (γ_1, γ_2), and BPZ-measured photo- z z_B to calculate the SC correlations as in Eqs. (11) and (12). We tested the signal drop Q s of Eqs. (13) and (14) with our photo- z PDF model and with true- z from simulation (van den Busch et al. 2020). We compared the results using MICE2 gold samples (which highly mimic the KiDS-1000 shear catalog galaxies) with magnification (Eq. (9)) and without magnification. For the MICE2 galaxies with magnification, we tested how it would bias the IA measurement and proved that when the magnification effect is also included in the model, IA can be measured in an unbiased way. The validations will be shown later in our results in more detail in Appendix A.

4. Measurements

We show the estimation of the signal-drops for lensing and IA due to the SC selection (as in Eqs. (13) and (14)), namely, the lensing-drop Q^{Gg} and the IA-drop Q^{Ig} in Fig. 4. They are responsible for the lensing-IA separation later in Fig. 6, following Eqs. (15) and (16). We followed the processes in Yao et al. (2020a,b) and adopted a bi-Gaussian photo- z probability distribution function (PDF) model with a secondary peak representing the photo- z outlier problem. We require the PDF model to have the same mean- z as in Fig. 3, while closest describing the projection from $n^{\text{P}}(z^{\text{P}})$ to $n(z)$. We will also show, for the first time, how the assumed photo- z PDF model can affect the results in the next section, with more details shown in Appendix A.

⁷ The Dark Energy Survey, <https://www.darkenergysurvey.org/>

⁸ <https://www.eso.org/qi/>

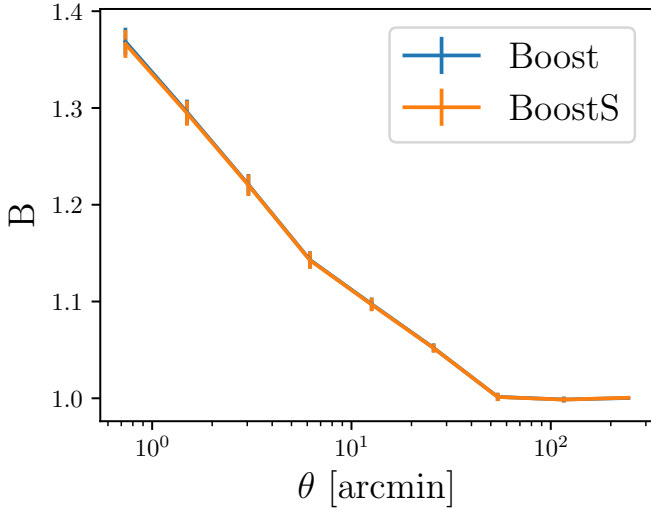


Fig. 5. Boost factors for $w^{\gamma g^l}$ (blue) and $w^{\gamma g^l}_S$ (orange). Overlapping lines suggest the two signals are affected by the boost factor in almost the same way. We show the boost factor is significant at small scales for the SC observables.

We calculate the SC correlation function estimator,

$$w^{\gamma g}(\theta) = B(\theta) \frac{\sum_{\text{ED}} w_j \gamma_j^+}{(1 + \bar{m}) \sum_{\text{ED}} w_j} - \frac{\sum_{\text{ER}} w_j \gamma_j^+}{(1 + \bar{m}) \sum_{\text{ER}} w_j}, \quad (24)$$

to obtain the measurements of $w^{\gamma g}$ and $w^{\gamma g}_S$ from the tangential shear of each galaxy γ_j^+ . Here we sum over the ellipticity-density pairs (\sum_{ED}) and the ellipticity-random pairs (\sum_{ER}) in an annulus centered on θ , where the shear weight, w_j , of the j -th galaxy and the average multiplicative bias, \bar{m} , are accounted for. The estimator is binned in angular θ space, with nine logarithmic bins from 0.5 to 300 arcmin. We used the averaged multiplicative bias \bar{m} from averaging over the three z -bins, weighted by the effective galaxy number density. This gives $\bar{m} = -0.0036$.

We account for the impact of the boost factor (Mandelbaum et al. 2005; Singh et al. 2017b; Joachimi et al. 2021), which is B in Eq. (24). It is defined as:

$$B(\theta) = \frac{\sum_{\text{ED}} w_j}{\sum_{\text{RD}} w_j}, \quad (25)$$

which is used to quantify the small-scale bias due to the clustering of lens galaxies and source galaxies (Bernardeau 1998; Hamana et al. 2002; Yu et al. 2015). This is because when applying the weight-correction to minimize the impact from shape noise, the summation over the pairs, \sum_{ED} , in the denominator of Eq. (24) can contain galaxy clustering information when the true- z of the source and lens overlaps. If $w_j = 1$, the summation of \sum_{ED} is proportional to $1 + w^{\text{eg}}$, where w^{eg} is the source-lens clustering correlation function. Such a bias will lead to a scale-dependent systematics, as the galaxy clustering correlation function is larger at small scales. We show the measurements of the boost factor for $w^{\gamma g^l}$ and $w^{\gamma g^l}_S$ as in Eqs. (11) and (12) and in Fig. 5. The fact that the boost factors for $w^{\gamma g^l}$ and $w^{\gamma g^l}_S$ are identical suggests this bias can be absorbed by the galaxy bias $b_{\text{g,eff}}$ parameter if magnification is absent ($g_{\text{mag}} = 0$), leading to an unbiased A_{IA} and A_{lens} . The impact from the boost factor can potentially break the linear galaxy bias assumption, but later in Fig. 6, we show the linear assumption is fine. The impact of the boost factor and magnification existing together is shown later in this paper.

In Fig. 6, we show the SC measurements. In the left panel, the measured shape-galaxy correlations $w^{\gamma g^l}$ are shown in blue: (1) the boost factor-ignored case ($B = 1$) is shown as blue crosses, while (2) the boost factor-corrected case is shown as blue up-triangles. With the SC selection Eq. (8), requiring $z_{\gamma}^{\text{P}} < z_{\text{g}}^{\text{P}}$ for each galaxy pair, the lensing component will drop to $Q^{\text{Gg}} \sim 0.3$ and the IA component will drop to $Q^{\text{lg}} \sim 0.85$ (for more details on Q^{Gg} and Q^{lg} , see Fig. 4 and Appendix A). Therefore, the selected correlations $w^{\gamma g}_S$ will drop to the orange down-triangles. Similarly, the boost factor-ignored case is shown as crosses.

The separated lensing-galaxy signal w^{Gg} and IA-galaxy signal w^{lg} (which is contaminated by magnification-shear signal $g_{\text{mag}} w^{\text{Gk}}$) are shown in the right panel of Fig. 6. The blue and orange curves are the theoretical predictions with the best-fit $\{A_{\text{IA}}, b_{\text{g,eff}}, g_{\text{mag}}\}$. For the fitting, we cut off the shaded regions at both large scales and small scales. The small scale cut at $\theta = 1$ arcmin is based on the linear galaxy bias assumption, as including the $\theta < 1$ arcmin data will make the fitting significantly worse (increasing the fitting χ^2 from 7.5 to 50, with degree-of-freedom changed from 8 to 10). We note this scale cut could include the impacts from the 3D non-linear galaxy bias (Fong & Han 2021) and other small-scale effects such as massive neutrinos or baryon feedback in the matter power spectrum (Hildebrandt et al. 2017; Asgari et al. 2021). We emphasize that these systematics will be absorbed by the effective galaxy bias parameter $b_{\text{g,eff}}$ (without breaking the scale-independent bias assumption) so that the IA amplitude will not be affected. As discussed previously in Yao et al. (2020a,b), the SC method requires significant separation between $w^{\gamma g^l}$ and $w^{\gamma g^l}_S$ to accurately get w^{Gg} and w^{lg} . Therefore, we introduced a large-scale cut at $\theta = 20$ arcmin due to insufficient separation for the left panel of Fig. 6.

Similarly, we measure the $\langle \gamma \kappa \rangle$ correlation with the estimator:

$$w^{\gamma \kappa}(\theta) = \frac{\sum_{ij} w_j \gamma_j^+ \kappa_i}{(1 + \bar{m}) \sum_{ij} w_j}, \quad (26)$$

where κ_i is the CMB lensing convergence in the i th pixel of the pixelized map, taking the pixel center for its (RA, Dec) coordinates, with $n_{\text{side}} = 2048$ in Healpy. The measured $w^{\gamma \kappa}$ values are shown in Fig. 7. The tangential shear is shown as blue dots. We also show the measurements with randomly shuffling galaxy positions and the shear in red crosses as a null test. We tested the 45 deg rotated cross-shear for both the above cases and they are consistent with zero. The theoretical prediction with the best-fit A_{lens} and A_{IA} are shown as the green curve. If one assumes there is no IA in the measurements and uses $A_{\text{IA}} = 0$, the theoretical values for the pure lensing signal are shown in orange.

We note in Fig. 7 that because we use the Wiener-filtered κ map from *Planck*, both the $w^{\gamma \kappa}$ measurements and the theoretical predictions are suppressed at small scales. The Wiener filter can significantly reduce the impact of the noise of the *Planck* lensing map and improve the S/N of the measurements.

Together with the measurements in Figs. 6 and 7, we obtain the observables of this work, which are the LHS terms of Eqs. (17)–(19). We used Jackknife resampling to obtain the covariance. 200 Jackknife regions are used, which is much larger than the length of the data vector (12), based on the analysis of Mandelbaum et al. (2006), Hartlap et al. (2007). The Jackknife regions are separated using the K-means algorithm `KMEANS_RADEC`⁹. The normalized covariance matrix is shown

⁹ https://github.com/esheldon/kmeans_radec

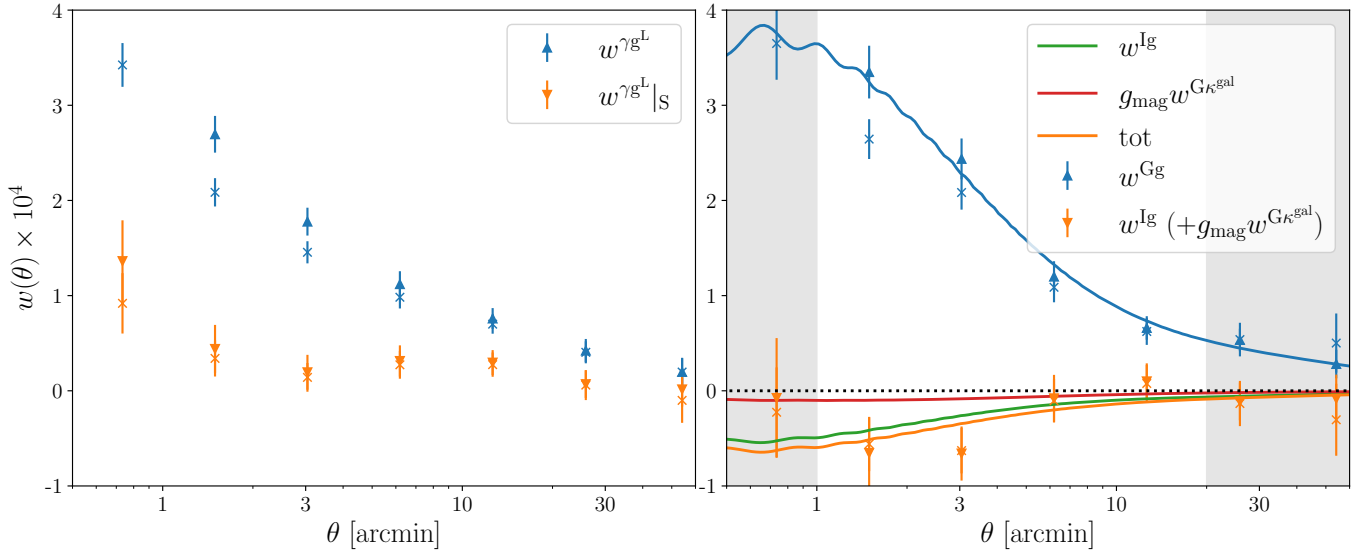


Fig. 6. Measurements of SC. Left panel shows the measurement of the two introduced observables $w^{\gamma g^L}$ and the one with the SC selection $w^{\gamma g^L}|_S$, while the corresponding 45-deg rotation test is consistent with 0 for both measurements. The significant separation of the two signals shows that SC is applicable. Right panel shows the separated lensing signal w^{Gg} and w^{Ig} (derived using Eqs. (15), (16), and Fig. 4), where the latter is contaminated by the magnification signal as shown in Eq. (16). The up- and down-triangles are the results that take the boost factor (Fig. 5) into consideration, while the crosses are the results that ignore this correction, setting $B = 1$. The curves are the theoretical value with the best-fit $\{A_{IA}, b_{g,eff}, g_{mag}\}$ of this work. The blue curve represents the separated lensing signal as in Eq. (17). Orange curve represents the total contribution of IA and magnification as in Eq. (18).

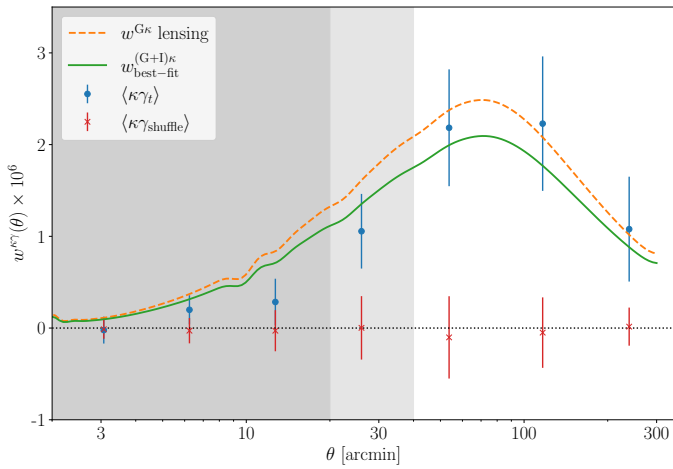


Fig. 7. Measurement of the cross-correlation between *Planck* convergence κ and KiDS-1000 shear γ , based on Eq. (19). The blue dots are the measurements using tangential shear, with the green curve showing the best-fit considering both lensing and IA, while the orange curve shows only the lensing-lensing component. The red crosses show the null test by randomly shuffling the shear galaxies. The 45-deg rotation tests for both the blue dots and the red dots are consistent with 0. The differently shaded regions correspond to our angular scale cuts at 2, 20 (default), and 40 arcmin.

in Fig. 8. We find strong anti-correlation between w^{Gg} and w^{Ig} as expected (Yao et al. 2020b). We note here in Fig. 8, w^{Ig} means the separated signal in the RHS of Eq. (16), including both the IA part and the contamination from magnification. There is no significant correlation between $w^{\gamma\kappa}$ and the other two observables. This covariance will be used in the Markov chain Monte Carlo (MCMC) to find the best-fit parameters of $\{A_{IA}, b_{g,eff}, g_{mag}, A_{lens}\}$, while all the other cosmological parameters are fixed to *Planck* as in Table 1.

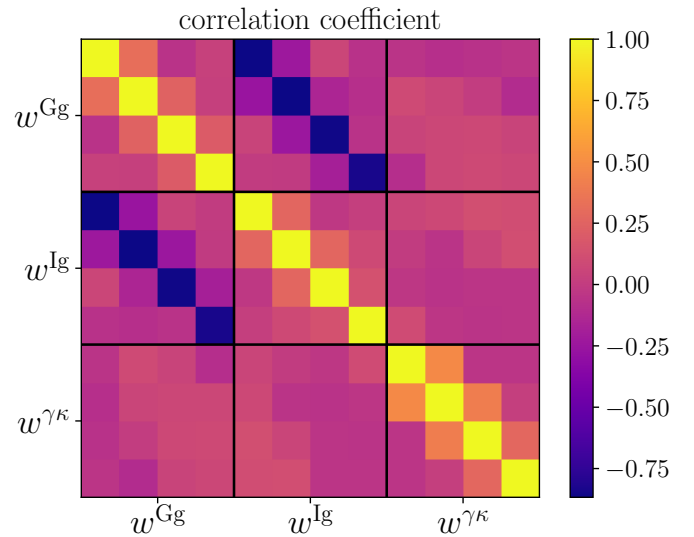


Fig. 8. Normalized covariance matrix (i.e., the correlation coefficient) used in this work. There is a strong anti-correlation that exists between the lensing-galaxy correlation w^{Gg} and the IA-galaxy correlation w^{Ig} (including the contamination from $w^{G\kappa^{gal}}$), as we found in our previous work. The covariance of the 12 data points is calculated from Jackknife resampling with 200 regions. We note the IA information is passed from $1 < \theta < 20$ [arcmin] for w^{Ig} to $20 < \theta < 300$ [arcmin] for $w^{\gamma\kappa}$ with the scale-independent A_{IA} assumption.

5. Results

5.1. Validation with MICE2

In this subsection, we apply the IA self-calibration to the MICE2 mock catalog to test the impact of the systematics and validate the recovery of the IA signal. The processes of the mock data are identical to the descriptions in Sect. 4, but only focusing on

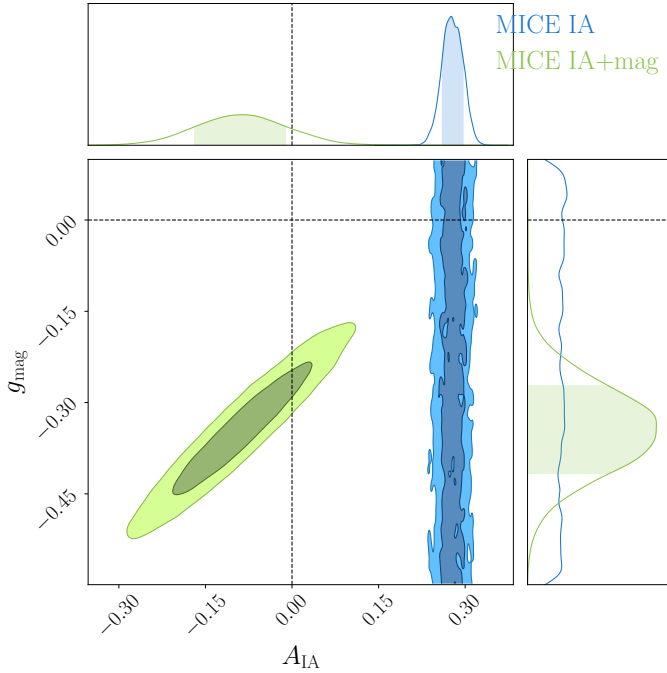


Fig. 9. Impact of the magnification signal on the IA measurement in MICE2. The green and blue contours are with and without magnification models, respectively. If the magnification model is used in the fitting, as in green, the IA amplitude A_{IA} is consistent with 0, which is the MICE2 input.

the self-calibration part. The measurements are similar to those of Fig. 6, so we chose to skip them. We performed the MCMC calculation using emcee (Foreman-Mackey et al. 2013). We considered flat priors in $-5 < A_{IA} < 5$, $0 < b_{g,eff} < 2$, and $-3 < g_{mag} < 3$.

5.1.1. Impact from magnification

We show how the magnification signal affects the original SC method (Zhang 2010b; Yao et al. 2020a,b) and the correction introduced in this work, focusing on the $g_{mag} - A_{IA}$ space.

In Fig. 9, we show that if magnification is not included in the modeling, g_{mag} is therefore not constrained. The existing magnification signal will be treated as the IA signal, leading to a non-vanishing $A_{IA} \sim 0.3$, which significantly deviates from the MICE2 input $A_{IA} = 0$. When the magnification model is included in the analysis, A_{IA} is then consistent with 0. This demonstrates the importance of including the magnification model in the SC analysis with high- z data. The results are also summarized later in the comparisons in Fig. 11 for MICE2, and in Fig. 14 for KiDS data.

We note that in the green case of Fig. 9 that considered both IA and magnification, g_{mag} and A_{IA} strongly degenerate. Therefore the constraining power in A_{IA} has a significant loss compared with the blue case, which ignores magnification. This degeneracy can be broken in the future with higher S/N in the observables. This is because the shape of w^{lg} and w^{Gk} are different at small scales for correlation functions as in Fig. 6, and on large scales for power spectra as in Fig. 2. The IA-model dependency will be discussed later with other results. Based on the above analysis, we draw the conclusion that it is important to include magnification modeling for SC when using high- z data.

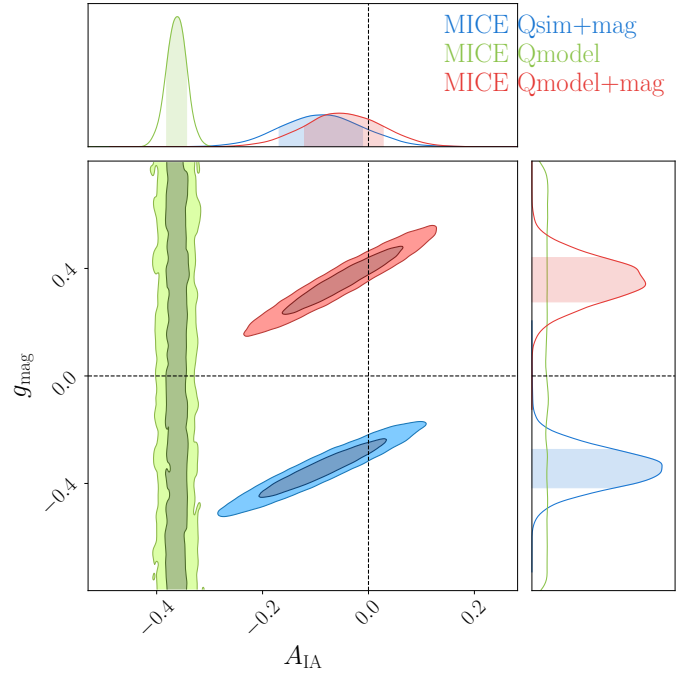


Fig. 10. Impact from photo- z PDF model bias. The blue case uses photo- z from the BPZ algorithm and true- z for each galaxy to calculate Eq. (A.7) and the resulting Q^{Gg} and Q^{lg} , which are the “sim” cases in Fig. A.1. This A_{IA} is consistent with 0, which is the MICE2 input. The green case uses the bi-Gaussian photo- z model for the calculation, which are the “model” cases in Fig. A.1, while ignoring the magnification contribution. This lead to unconstrained g_{mag} and biased A_{IA} . In the red case, which also uses the photo- z model, but includes the magnification model, the resulting A_{IA} is still consistent with 0, with the bias from photo- z model error absorbed by g_{mag} .

5.1.2. Impact from modeling $p(z|z^P)$

Since the SC selection Eq. (8) plays an important role in the lensing-IA separation process, it is crucial to understand how the following aspects affect SC: (1) the quality of the photo- z z^P , (2) the true redshift distribution $n(z)$, and (3) the link between them $p(z|z^P)$. The quality of photo- z and the reconstruction of $n(z)$ has been studied thoroughly for KiDS data (Kuijken et al. 2019; van den Busch et al. 2020, 2022; Hildebrandt et al. 2021); therefore, we trust these results and leave the alternative studies for SC to future works. The uncalibrated PDF that projects $z^P \rightarrow z$, on the other hand, has some known problems, for example, when Probability Integral Transform (PIT) is applied (Newman & Gruen 2022; Hasan et al. 2022).

In this work, we use a bi-Gaussian PDF model to project the photo- z distribution $n^P(z^P)$ to the SOM redshift distribution $n(z)$, which are shown in Fig. 3. This modeling ignores the potential differences for galaxies in the same z -bin (Peng et al. 2022; Xu et al. 2023). However, this is an alternative process, considering the PDF problem for a single galaxy. This analytical approach is also much faster in calculation than using different PDFs for different galaxies.

We used Fig. 10 to demonstrate how large this photo- z PDF modeling bias is with different approaches. We used a MICE2 simulation with galaxy number density affected by magnification. When the SC calculation uses true- z to calculate the signal drops Q^{Gg} and Q^{lg} , and the magnification model is also considered, we find the resulting A_{IA} is consistent with 0, which is the MICE2 input. The scatter on A_{IA} is ~ 0.1 , thanks to the

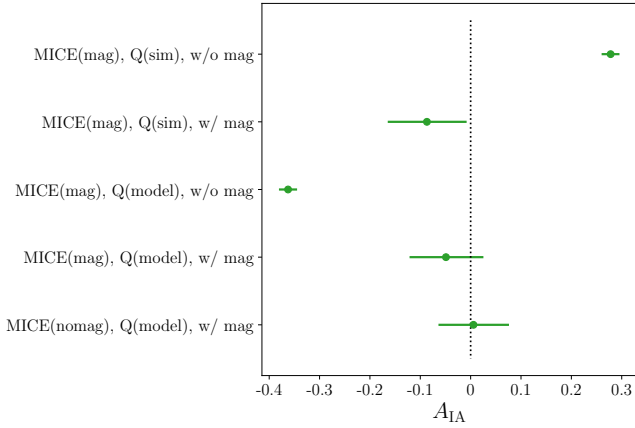


Fig. 11. Validation for our SC method with MICE2 simulation. The mock does not have IA implemented; therefore, $A_{IA} = 0$ is expected. The results are shown in green, with “MICE(mag)” meaning magnification is included in the MICE simulation, while “MICE(nomag)” means magnification is not included, “Q(sim)” and “Q(model)” mean if the signal drops Q values are calculated from true- z from simulation or photo- z PDF model, and “w/o mag” and “w/ mag” show if the case includes magnification model in the fitting process. The upper two data points are the results from Fig. 9, showing the impact of the modeling magnification. The second to fourth data points are the results from Fig. 10, showing the impact of Q calculation using different PDFs. The fourth data point corresponds to our fiducial analysis carried out later for the KiDS data, with potential bias $\Delta A_{IA} < 0.1$. The bottom data is a reference case assuming no magnification effects in the data, corresponding to our previous work Yao et al. (2020a,b).

noiseless shapes in MICE2. If the Q s are calculated with the assumed photo- z PDF model (based on Fig. 3), without including the magnification model, then A_{IA} will be biased towards the negative direction. We proved with our fiducial analysis that, even if there a bias in Q^{Gg} exists due to the assumed photo- z model, as long as the magnification model is used, this bias will be absorbed by the g_{mag} parameter, so that the IA amplitude A_{IA} is unbiased (consistent with 0 in the MICE2 case). The results are also shown later in the comparisons in Fig. 11 for MICE2, and in Fig. 14 for KiDS data.

We note that it is not guaranteed that the bias coming from photo- z modeling will be absorbed by the magnification parameterization for all data sets. The above tests only validate this approach with KiDS or KiDS-like data that the residual bias $|\Delta A_{IA}| < 0.1$. However, it is not an essential problem for SC. In the future, if the photo- z outlier problem (or the redshift-color degeneracy problem) can be understood better, then a more reliable photo- z model can be used for our SC study. Alternatively, if the photo- z algorithms can give unbiased PDFs for each galaxy, this problem can also be directly solved. Direct approaches such as multiple SOM $n(z)$ for high-resolution photo- z bins (rather than the total five bins in the current KiDS data Asgari et al. (2021)) or using galaxy clustering to derive a scatter matrix to describe the PDF $p(z|z^P)$ (Xu et al. 2023) can be investigated in the future. The combination between a color-based method and a clustering-based method (Aldarcon et al. 2020) can be even more promising in improving this aspect.

5.2. Inference on real data

With the above demonstration that our treatments for magnification and photo- z PDF are appropriate and the resulting bias

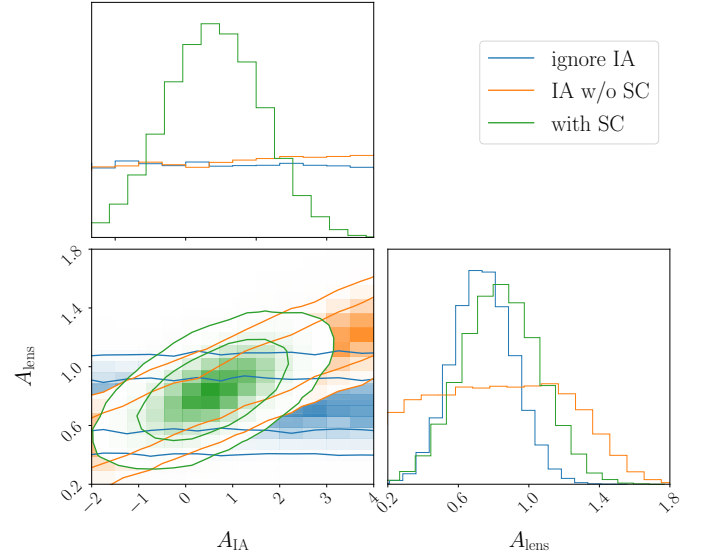


Fig. 12. Constraints on lensing amplitude A_{lens} and the IA amplitude A_{IA} , with three different methods: assuming there is no IA in the measured w^{γ} (blue), considering the impact of IA with conventional IA model but do not use SC (orange), and using SC to subtract IA information and constrain together with the CMB lensing cross-correlation (green). When IA is ignored, A_{IA} is unconstrained. The similar height and width of A_{lens} PDFs between blue and green prove that by including SC, the $A_{IA} - A_{lens}$ degeneracy can be efficiently broken so that the constraining power loss in A_{lens} is very small.

in A_{IA} is very small, with ($|\Delta A_{IA}| < 0.1$ and $< 1\sigma$ as shown in Fig. 11), we go on to apply SC to KiDS data and its cross-correlation with *Planck* lensing. We show the analysis of the following three situations: (1) case of ignore IA: we only used the observed w^{γ} , while including A_{lens} in the fit and ignoring the contamination by IA (by setting $A_{IA} = 0$); (2) case of IA w/o SC: we only used the observed w^{γ} , but consider both A_{lens} and A_{IA} following Eq. (19); (3) case of SC: we used both w^{γ} in Fig. 7 and the SC correlations in Fig. 6. Both the CMB lensing amplitude A_{lens} and the nuisance parameters $\{A_{IA}, b_{g,eff}, g_{mag}\}$ are used in the analysis, following Eqs. (17)–(19).

The results of these simulations are shown in Fig. 12. We use flat priors in $0 < A_{lens} < 2$, $-5 < A_{IA} < 5$, and for the IA self-calibration nuisance parameters we use $0 < b_{g,eff} < 4$, $-5 < g_{mag} < 5$. For case 1 (ignore IA), shown in blue, A_{IA} is unconstrained in the fitting, giving the best-fit $A_{lens} = 0.74^{+0.18}_{-0.17}$. For case 2 (IA w/o SC, when we consider the existence of IA and apply the IA model as in Eq. (7), but do not use the measurements from SC (Fig. 6 and Eqs. (17) and (18))), there will be a strong degeneracy between A_{lens} and A_{IA} , as shown in orange. There is a significant loss of constraining power in the lensing amplitude, with the best-fit $A_{lens} = 0.79^{+0.43}_{-0.46}$ and $A_{IA} = 0.47^{+3.11}_{-3.47}$. For case 3 (with SC), the introduced measurements of w^{Gg} and w^{lg} has the capacity to not only break the degeneracy between A_{lens} and A_{IA} (see Eqs. (17)–(19)), but also to bring more constraining power to A_{IA} , so that the best fit of A_{lens} will be both unbiased (according to the validation using simulation) and have significantly improved constraining power. The best-fit values are $A_{lens} = 0.84^{+0.22}_{-0.22}$, $A_{IA} = 0.60^{+1.03}_{-1.03}$, $b_{g,eff} = 0.88^{+0.06}_{-0.06}$, and $g_{mag} = -0.30^{+1.60}_{-1.62}$. In Fig. 12, we only show A_{IA} and A_{lens} , which are the focus of this work, while $b_{g,eff}$ and g_{mag} are only related with the SC observables but not CMB lensing. Also, as discussed in Yao et al. (2020b), the existence of the effective galaxy

bias $b_{g,\text{eff}}$ can also absorb some systematics (thus, it may be a biased bias), leaving the constraint on A_{IA} unbiased (as shown in Fig. 11). For example, we tested whether when magnification is absent, the effect of the boost factor will be fully absorbed by $b_{g,\text{eff}}$, giving unbiased values for A_{IA} and A_{lens} . The effective galaxy bias could also absorb the differences in the assumed fiducial cosmology, with $b_{g,\text{eff}} \sim 1.24$ with KiDS COSEBI cosmology, for example. The redshift distribution $n(z)$ can differ slightly when accounting for (or not) the lensing weight (considering the lensing or clustering part in the galaxy-shape correlation), with a ~ 0.024 difference in the mean- z , which can lead to $\sim 8\%$ difference in the theoretical lensing signal and $\sim 2\%$ difference in the theoretical IA signal. Other unaddressed sources of systematics such as baryonic feedback and massive neutrinos could have similar effects. We can also see from the validation using MICE data that although the resulting $b_{g,\text{eff}}$ is lower than the expectation, the A_{IA} result is unbiased. The g_{mag} result also resides in a reasonable range, considering the KiDS i -band magnitude (Kuijken et al. 2019) and comparing it with Duncan et al. (2014). The above three cases of IA treatments are also summarized later in Figs. 13 and 14 together with more tests and other works.

The corresponding best-fit curves are shown in Figs. 2 and 6 with $A_{\text{IA}} = 0.60^{+1.03}_{-1.03}$, $b_{g,\text{eff}} = 0.88^{+0.06}_{-0.06}$, and $g_{\text{mag}} = -0.30^{+1.60}_{-1.62}$. Even though the impact of magnification is comparable to the IA signal, we can see in both the angular power spectrum and correlation function that the shapes of IA and magnification are different. For example, as shown in Fig. 6, the tidal alignment model w^{lg} and magnification $g_{\text{mag}} w^{\text{Gk}}$ are comparable at large scales, but differ at small scales. Therefore, in principle, the degeneracy between IA and magnification can be broken for future data with higher S/N, so that the shape or slope information of the observables can be used. The current degeneracy is due to the low S/N so that the amplitudes of A_{IA} and g_{mag} degenerate. Furthermore, if a more complicated IA model is used, for example, as in Blazek et al. (2019), Abbott et al. (2022), the small-scale IA will be different. Based on the study of Shi et al. (2021), for a wide range of stellar mass, the small-scale IA should have a higher amplitude (either a direct raise in the amplitude or a “drop-raise” pattern as we go down to smaller scales) than the current model so that the IA-magnification degeneracy can be broken further. The appropriate IA model will require studies in many aspects and with higher S/N in the measurements. Thus, we leave this topic to a future work.

We investigate how different choices can change our results. We first compare the different scale cuts for w^{K} . Besides the baseline analysis of $A_{\text{lens}} = 0.84^{+0.22}_{-0.22}$ with $\theta > 20$ arcmin, two more tests are made with a larger scale cut of $\theta > 40$ arcmin and a smaller scale cut of $\theta > 2$ arcmin, as shown in Fig. 7, which give us $A_{\text{lens}} = 0.97^{+0.25}_{-0.25}$ and $A_{\text{lens}} = 0.77^{+0.21}_{-0.22}$, respectively. The comparisons are shown in Fig. 13. The large-scale lensing amplitude is higher than the small-scale one, which agrees with the finding in Planck Collaboration VIII (2020) and other works on cross-correlations (Sun et al. 2022). In this work, we only report this large-scale versus small-scale difference. However, the current S/N of the correlation of the CMB convergence and galaxy shear and the model assumptions do not allow us to investigate further on this topic. Similarly, the impact from point-source subtraction errors in the CMB lensing map (Planck Collaboration VIII 2020) is negligible ($\leq 0.2\%$) in this cross-correlation analysis.

We then compare the different choices in the SC method. We find that if the magnification model is ignored in the analysis, the existing magnification signal in the data will be treated as an IA signal, leading to an overestimated $A_{\text{IA}} = 0.81^{+0.36}_{-0.41}$

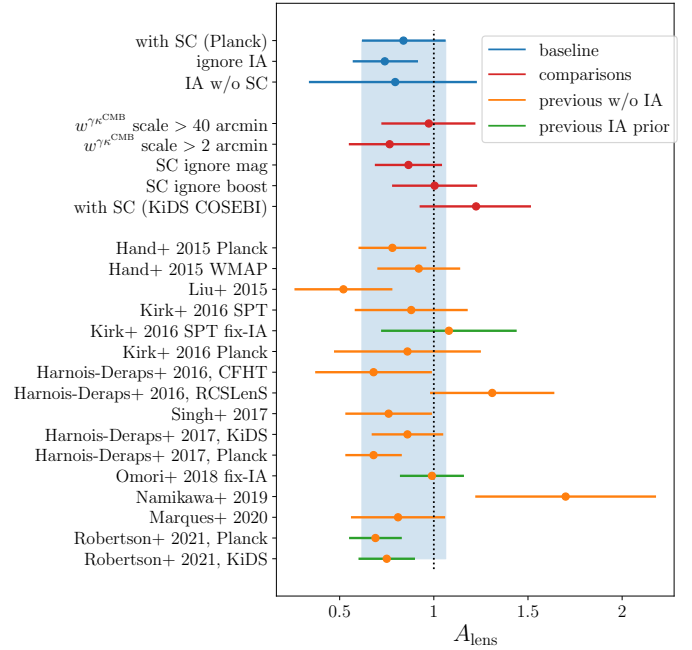


Fig. 13. Comparisons of the constraints on A_{lens} with previous measurements. Our baseline analysis “with SC” is consistent with 1. We also show some cases where IA is ignored in the analysis and if IA is considered but the $A_{\text{IA}} - A_{\text{lens}}$ degeneracy is not broken with SC. These main results in blue are similar to what is shown in Fig. 12. We show tests with different scale cuts and different treatments to magnification, the boost factor, and different (KiDS) fiducial cosmologies in red. We make a comparison with other works, divided into that ignoring IA (orange) and that assuming a strong prior of IA (green). We note that for different works, the different fiducial cosmologies (the “Planck”, “WMAP”, and “KiDS” labels on the y-axis) can lead to $\sim 10\%$ difference in A_{lens} .

an overestimated $A_{\text{lens}} = 0.87^{+0.18}_{-0.18}$. On the other hand, we previously argued that when magnification is absent, the impact from the boost factor will be purely absorbed by the effective galaxy bias, $b_{g,\text{eff}}$, leaving A_{IA} and A_{lens} unbiased. Unfortunately, this does not hold anymore when magnification is present: if the boost factor is not corrected, all the parameters will be biased as follows $A_{\text{IA}} = 1.86^{+1.01}_{-1.05}$, $b_{g,\text{eff}} = 0.67^{+0.06}_{-0.06}$, $A_{\text{lens}} = 1.00^{+0.23}_{-0.23}$ and $g_{\text{mag}} = 1.55^{+1.28}_{-1.31}$. We include the comparisons of A_{lens} and A_{IA} for the above-described cases in Fig. 13 and 14 and emphasize the importance of taking magnification and boost factor into consideration. We also show the impact of the assumed fiducial cosmology: if the fiducial cosmology is switched from Planck to KiDS-1000 COSEBI as in Table 1, both A_{lens} and A_{IA} will change as shown in Fig. 13 (bottom: red) and 14 (bottom: blue).

With the above results in simulation and data, summarized in Figs. 11, 13, and 14, we show that our measurements on A_{IA} and A_{lens} are unbiased with regard to magnification, the boost factor, and the assumed photo- z PDF model. These are new developments that consider the existence of magnification at high redshift $z \sim 1$, beyond the study of Yao et al. (2020b).

Additionally, we compare our analysis with previous works. The comparisons of A_{lens} are shown in Fig. 13. We find that most of the previous works have ignored the IA contamination (Hand et al. 2015; Liu & Hill 2015; Kirk et al. 2016; Harnois-Déraps et al. 2016, 2017; Singh et al. 2017a; Namikawa et al. 2019; Marques et al. 2020). For the ones that considered IA, they either fixed the IA amplitude (Kirk et al. 2016; Omori et al. 2019) or used a strong prior (Robertson et al. 2021)

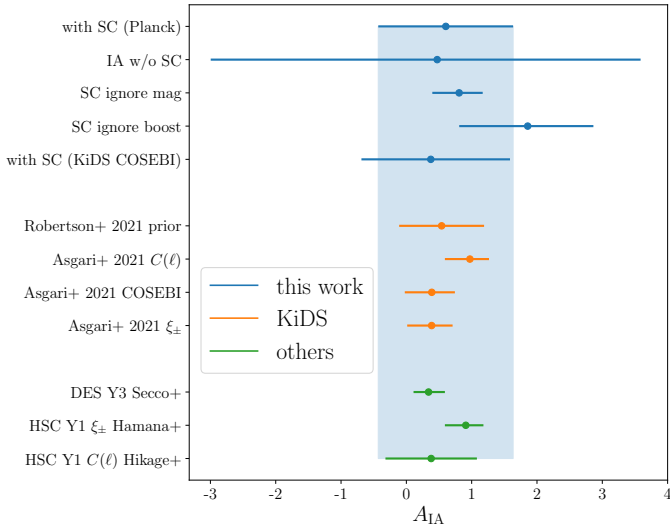


Fig. 14. Comparisons of the constraints on A_{IA} . We show the results of this work in blue, which contains our fiducial analysis with SC applied and the comparisons of (1) without SC, (2) with SC but ignoring magnification, (3) with SC but ignoring the boost factor, and (4) switching to the KiDS fiducial cosmology. We show comparisons with other works using KiDS-1000 data in orange and some works using DES or HSC data in green.

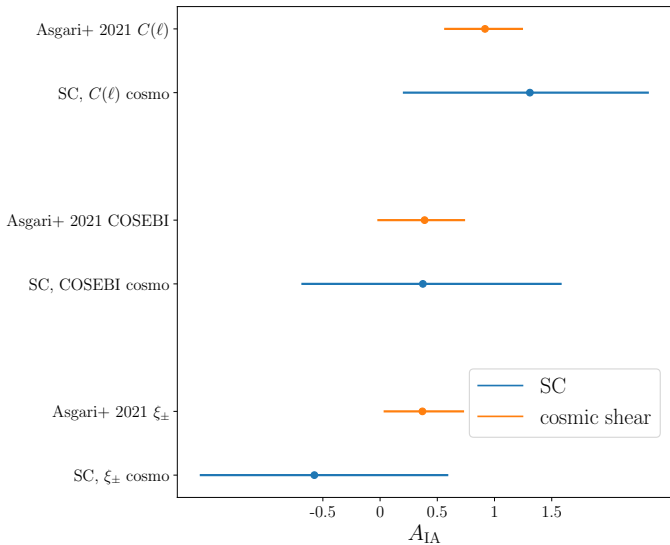


Fig. 15. Comparisons of A_{IA} between SC-subtracted results (blue) and cosmic shear tomography subtracted results (orange) with cosmologies from different two-point statistics. The cosmologies are shown in Table 1.

to break the degeneracy between A_{lens} and A_{IA} , which would otherwise cause a strong loss in constraining power, as we show in Fig. 12. We are the first to directly achieve the IA amplitude measurement within the same data and break the lensing-IA degeneracy. Our baseline analysis is consistent with most of the previous results, showing the contamination from IA is not significant, mainly due to the total S/N of CMB lensing-galaxy shear cross-correlation is only at $3 \sim 5 \sigma$ level at the current stage. However, the correct treatment for IA will be more and more important in the future with the advent of stage IV cosmic shear surveys and CMB observations.

Comparisons of the A_{IA} constraint with other results using KiDS-1000 data are shown in Fig. 14, including the prior assumed in Robertson et al. (2021) and the cosmic shear tomography constraint in Asgari et al. (2021). Although the redshift range is slightly different, the above works demonstrate consistent results for A_{IA} . These comparisons will become more interesting for the next-stage observations.

As an extended study, we investigate how the choice of fiducial cosmology affects the SC results, namely A_{IA} . In Fig. 14, we show the results with the fiducial *Planck* cosmology and the KiDS-1000 two-point correlation function ξ_{\pm} best-fit cosmology. We further compare the results with the KiDS-1000 band power $C(\ell)$ cosmology and the COSEBIs cosmology in Fig. 15. The results from Asgari et al. (2021; shown in orange) are arranged in increasing order from bottom to top. We find that when assuming the same cosmology, the SC results (shown in blue) also follow the same (weak) trend; meanwhile, they agree very well with the cosmic shear results. We note the SC results will provide extra information in constraining IA in cosmic shear in the future.

6. Summary

In this work, we carry out the first application of the self-calibration (SC) method of intrinsic alignment (IA) of galaxies to its cosmological application. We proved that with SC, the lensing-IA degeneracy could be efficiently broken, namely, in this CMB lensing \times galaxy shear cross-correlation work, it means breaking the degeneracy between the lensing amplitude, A_{lens} , and the IA amplitude, A_{IA} . We show that for previous treatments, IA values are either ignored or being considered with a strong assumed prior on A_{IA} . We demonstrate in Figs. 12–14 that with SC to break the degeneracy, the constraining power in both A_{lens} and A_{IA} is preserved.

We demonstrate that the proper angular scale cuts on w^{kY} are important. Our baseline analysis using information from $\theta > 20$ arcmin gives $A_{lens} = 0.84^{+0.22}_{-0.22}$. If we use information only at larger scales with $\theta > 40$ arcmin, the constraint is $A_{lens} = 0.97^{+0.25}_{-0.25}$. If we include information at much smaller scales with $\theta > 2$ arcmin, the constraint is $A_{lens} = 0.77^{+0.21}_{-0.22}$. At the current stage, these results do not differ significantly from each other (even considering they are strongly correlated), as shown in Fig. 13. However, we note that these differences at different scales also exist in other works, such as Planck Collaboration VIII (2020) and Sun et al. (2022). Therefore, we emphasize the importance of understanding the possible systematics at different scales for future studies with higher S/N, possibly using updated maps with more data (Carron et al. 2022) or in combination with other observations (Robertson et al. 2021; Darwish et al. 2021).

Comparing our CMB lensing amplitude, A_{lens} , with other works in Fig. 13, we found consistent results with different treatments of IA throughout almost all the works. We conclude that IA is not a significant source of systematics for the current stage. However, it will soon become more important with the stage IV observations. Nevertheless, we emphasize that the correct treatment to break the lensing-IA degeneracy is very important for maintaining the cosmological constraining power. Our constraint on the IA amplitude A_{IA} in Fig. 14 is also consistent with the existing analysis on IA with KiDS-1000 data. We note that the SC-subtracted IA information can be used as extra constraining power for any of these analyses.

On the technique side, we further developed the SC method considering more sources of systematics beyond

Yao et al. (2020b). We show that at $z \sim 1$, the impact of galaxy shear \times cosmic magnification component $w^{G_{\text{gal}}}$ contaminates the separated IA \times galaxy number density signal w^{lg} and is non-negligible, as shown in Figs. 2 and 6. We use Eqs. (16) and (18) to show how the magnification term enters our observable and how we include it in the theory as a correction. We show in Figs. 13 and 14 that the correction of magnification is important when applying SC to higher redshift data in order to get the correct constraint on IA. We also discuss the fact that with the contamination from magnification, the boost factor can no longer be absorbed by the effective galaxy bias $b_{\text{g,eff}}$, and need to be accounted for correctly, as shown in Eqs. (24) and (25) and Figs. 6, 13, and 14.

We also validated our analysis with MICE2 simulation, focusing on two aspects: (1) how well magnification model can mitigate the contamination from the magnification-shear signal and (2) whether the assumed photo- z PDF model (which is used to calculate the signal drop Q^{Gg} and Q^{lg}) bias the IA measurement. With the strong constraining power from MICE2 with no shape noise, we can show in Fig. 11 that, when the magnification model is included in the analysis, the IA amplitude can be obtained correctly (consistent within 1σ range of 0, which is the input of MICE2). Additionally, the bias from the assumed photo- z model is negligible when the magnification model is used, as the effective magnification prefactor g_{mag} will absorb the introduced error, leaving the residual bias $|\Delta A_{\text{IA}}| < 0.1$. This validation is suitable for KiDS and KiDS-like data only. Therefore, we emphasize the importance of including the magnification model and advanced photo- z modeling in the SC analysis, especially for future high- z surveys such as LSST, Euclid, WFIRST, and CSST. We further notice the contamination from magnification will make SC no longer an IA-model-independent method, therefore, SC is more suitable for low- z data when considering alternative IA models.

In comparison with our first measurements with the KV-450 data (Yao et al. 2020a), a lot of improvements have been made to the SC method, including: (1) the covariance, the galaxy bias, the scale-dependency for the lensing-drop Q^{Gg} , the IA-drop Q^{lg} , and appropriate scale-cuts, which have been introduced in Yao et al. (2020b); (2) the boost factor, the cosmic magnification, and the photo- z PDF modeling, which are introduced in this work; (3) its first validation using simulation, and its first application to cosmology in order to break the lensing-IA degeneracy, introduced in this work. With these improvements, we manage to achieve consistent IA results between SC and cosmic shear, as shown in Fig. 15, while previously we got $A_{\text{IA}} = 2.31^{+0.42}_{-0.42}$ with the old version of SC (Yao et al. 2020a) and $A_{\text{IA}} = 0.981^{+0.694}_{-0.678}$ for cosmic shear (Hildebrandt et al. 2020) with KV-450 data.

The SC-obtained A_{IA} is consistent with the MICE-input IA as well as with the KiDS cosmic shear results when applied to the data, for instance, from Asgari et al. (2021). It is also consistent with the other CMB lensing works, such as Robertson et al. (2021), and g_{mag} is also in reasonable agreement with the work of Duncan et al. (2014). Nevertheless, our results still suffer from an unrealistically low effective galaxy bias of $b_{\text{g,eff}} = 0.88$, which is different from the results presented in our previous work (Yao et al. 2020b). We discuss the possibility that this value may absorb the contribution from (1) fiducial cosmology, (2) lensing weight in $n(z)$, (3) insufficient modeling in non-linear galaxy bias, baryonic effects, and massive neutrinos, (4) incorrect photo- z versus true- z connection (discussed in Appendix A), and (5) possible other sources of systematics. We emphasize these complications and leave this point for further discussion in future studies.

We note that other systematics may be at work other than the galaxy bias, such as the beyond Limber approximation (Fang et al. 2020), non-flat Λ CDM (Yu et al. 2021), or selection bias on shear measurements (Li et al. 2021). However, these have either a much smaller impact compared to IA or they are strongly reduced due to our scale cuts. Thus, these remain beyond the scope of this paper and may be the topic of a future work.

Acknowledgements. The authors thank Yu Yu, Hai Yu, Jiaxin Wang for useful discussions. This work is supported by National Key R&D Program of China No. 2022YFF0503403. JY, HYS, PZ and XL acknowledge the support from CMS-CSST-2021-A01, CMS-CSST-2021-A02 and CMS-CSST-2021-B01. JY acknowledges the support of the National Science Foundation of China (12203084), the China Postdoctoral Science Foundation (2021T140451), and the Shanghai Post-doctoral Excellence Program (2021419). HYS acknowledges the support from NSFC of China under grant 11973070, the Shanghai Committee of Science and Technology grant No. 19ZR1466600 and Key Research Program of Frontier Sciences, CAS, Grant No. ZDBS-LY-7013. PZ acknowledges the support of the National Science Foundation of China (11621303, 11433001). XL acknowledges the support of NSFC of China under Grant No. 12173033, 11933002, 11803028, YNU Grant No. C176220100008, and a grant from the CAS Interdisciplinary Innovation Team. BJ acknowledges support by STFC Consolidated Grant ST/V000780/1. MB is supported by the Polish National Science Center through grants no. 2020/38/E/ST9/00395, 2018/30/E/ST9/00698, 2018/31/G/ST9/03388 and 2020/39/B/ST9/03494, and by the Polish Ministry of Science and Higher Education through grant DIR/WK/2018/12. HH is supported by a Heisenberg grant of the Deutsche Forschungsgemeinschaft (Hi 1495/5-1) as well as an ERC Consolidator Grant (No. 770935). TT acknowledges support from the Leverhulme Trust. AW is supported by an European Research Council Consolidator Grant (No. 770935). ZY acknowledges support from the Max Planck Society and the Alexander von Humboldt Foundation in the framework of the Max Planck-Humboldt Research Award endowed by the Federal Ministry of Education and Research (Germany). The computations in this paper were run on the π 2.0 cluster supported by the Center for High Performance Computing at Shanghai Jiao Tong University. The codes JY produced for this paper were written in Python. JY thanks all its developers and especially the people behind the following packages: SCIPY (Jones et al. 2001), NUMPY (van der Walt et al. 2011), ASTROPY (Astropy Collaboration 2013) and MATPLOTLIB (Hunter 2007), TreeCorr (Jarvis et al. 2004), CCL (Chisari et al. 2019), CAMB (Lewis et al. 2000), Healpy (Górski et al. 2005; Zonca et al. 2019), emcee (Foreman-Mackey et al. 2013), fitsio (<https://github.com/esheldon/fitsio>), kmeans_radec (https://github.com/esheldon/kmeans_radec), corner (Foreman-Mackey 2016), ChainConsumer (<https://github.com/Samreay/ChainConsumer>). The KiDS-1000 results in this paper are based on data products from observations made with ESO Telescopes at the La Silla Paranal Observatory under programme IDs 177.A-3016, 177.A-3017 and 177.A-3018, and on data products produced by Target/OmegaCEN, INAF-OACN, INAF-OAPD, and the KiDS production team, on behalf of the KiDS consortium. Author contributions: All authors contributed to the development and writing of this paper. The authorship list is given in three groups: the lead authors (JY, HS, PZ, XL) followed by two alphabetical groups. The first alphabetical group includes those who are key contributors to both the scientific analysis and the data products. The second group covers those who have either made a significant contribution to the data products, or to the scientific analysis.

References

- Abbott, T. M. C., Aguena, M., Alarcon, A., et al. 2022, *Phys. Rev. D*, **105**, 023520
- Alarcon, A., Sánchez, C., Bernstein, G. M., & Gaztañaga, E. 2020, *MNRAS*, **498**, 2614
- Amon, A., Gruen, D., Troxel, M. A., et al. 2022, *Phys. Rev. D*, **105**, 023514
- Asgari, M., Lin, C.-A., Joachimi, B., et al. 2021, *A&A*, **645**, A104
- Astropy Collaboration (Robitaille, T. P., et al.) 2013, *A&A*, **558**, A33
- Bartelmann, M. 1995, *A&A*, **298**, 661
- Bartelmann, M., & Schneider, P. 2001, *Phys. Rep.*, **340**, 291
- Begeman, K., Belikov, A. N., Boxhoorn, D. R., & Valentijn, E. A. 2013, *Exp. Astron.*, **35**, 1
- Benitez, N. 2000, *ApJ*, **536**, 571
- Bernardeau, F. 1998, *A&A*, **338**, 375
- Blazek, J., Vlah, Z., & Seljak, U. 2015, *J. Cosmol. Astropart. Phys.*, **8**, 015

- Blazek, J. A., MacCrann, N., Troxel, M. A., & Fang, X. 2019, *Phys. Rev. D*, **100**, 103506
- Bridle, S., & King, L. 2007, *New J. Phys.*, **9**, 444
- Brown, M. L., Taylor, A. N., Hambly, N. C., & Dye, S. 2002, *MNRAS*, **333**, 501
- Carretero, J., Castander, F. J., Gaztañaga, E., Crocce, M., & Fosalba, P. 2015, *MNRAS*, **447**, 646
- Carron, J., Mirmelstein, M., & Lewis, A. 2022, *J. Cosmol. Astropart. Phys.*, **2022**, 039
- Catelan, P., Kamionkowski, M., & Blandford, R. D. 2001, *MNRAS*, **320**, L7
- Chang, C., Wang, M., Dodelson, S., et al. 2019, *MNRAS*, **482**, 3696
- Chisari, N. E., Dunkley, J., Miller, L., & Allison, R. 2015, *MNRAS*, **453**, 682
- Chisari, N., Laigle, C., Codis, S., et al. 2016, *MNRAS*, **461**, 2702
- Chisari, N. E., Koukoufyllipas, N., Jindal, A., et al. 2017, *MNRAS*, **472**, 1163
- Chisari, N. E., Alonso, D., Krause, E., et al. 2019, *ApJS*, **242**, 2
- Crittenden, R. G., Natarajan, P., Pen, U.-L., & Theuns, T. 2001, *ApJ*, **559**, 552
- Crocce, M., Castander, F. J., Gaztañaga, E., Fosalba, P., & Carretero, J. 2015, *MNRAS*, **453**, 1513
- Croft, R. A. C., & Metzler, C. A. 2000, *ApJ*, **545**, 561
- Darwish, O., Madhavacheril, M. S., Sherwin, B. D., et al. 2021, *MNRAS*, **500**, 2250
- de Jong, J. T. A., Verdoes Kleijn, G. A., Boxhoorn, D. R., et al. 2015, *A&A*, **582**, A62
- Dong, F., Zhang, P., Zhang, L., et al. 2021, *ApJ*, **923**, 153
- Duncan, C. A. J., Joachimi, B., Heavens, A. F., Heymans, C., & Hildebrandt, H. 2014, *MNRAS*, **437**, 2471
- Erben, T., Hildebrandt, H., Miller, L., et al. 2013, *MNRAS*, **433**, 2545
- Fang, X., Krause, E., Eifler, T., & MacCrann, N. 2020, *J. Cosmol. Astropart. Phys.*, **2020**, 010
- Fong, M., & Han, J. 2021, *MNRAS*, **503**, 4250
- Foreman-Mackey, D. 2016, *J. Open Source Softw.*, **1**, 24
- Foreman-Mackey, D., Hogg, D. W., Lang, D., & Goodman, J. 2013, *PASP*, **125**, 306
- Fortuna, M. C., Hoekstra, H., Joachimi, B., et al. 2021, *MNRAS*, **501**, 2983
- Fosalba, P., Gaztañaga, E., Castander, F. J., & Crocce, M. 2015, *MNRAS*, **447**, 1319
- Giblin, B., Heymans, C., Asgari, M., et al. 2021, *A&A*, **645**, A105
- Górski, K. M., Hivon, E., Banday, A. J., et al. 2005, *ApJ*, **622**, 759
- Hamana, T., Colombi, S. T., Thion, A., et al. 2002, *MNRAS*, **330**, 365
- Hamana, T., Shirasaki, M., Miyazaki, S., et al. 2020, *PASJ*, **72**, 16
- Hand, N., Leauthaud, A., Das, S., et al. 2015, *Phys. Rev. D*, **91**, 062001
- Harnois-Déraps, J., Tröster, T., Hojjati, A., et al. 2016, *MNRAS*, **460**, 434
- Harnois-Déraps, J., Tröster, T., Chisari, N. E., et al. 2017, *MNRAS*, **471**, 1619
- Hartlap, J., Simon, P., & Schneider, P. 2007, *A&A*, **464**, 399
- Hasan, I. S., Schmidt, S. J., Schneider, M. D., & Tyson, J. A. 2022, *MNRAS*, **511**, 1029
- Heymans, C., Brown, M., Heavens, A., et al. 2004, *MNRAS*, **347**, 895
- Heymans, C., Tröster, T., Asgari, M., et al. 2021, *A&A*, **646**, A140
- Hikage, C., Oguri, M., Hamana, T., et al. 2019, *PASJ*, **71**, 43
- Hildebrandt, H., Viola, M., Heymans, C., et al. 2017, *MNRAS*, **465**, 1454
- Hildebrandt, H., Köhlinger, F., van den Busch, J. L., et al. 2020, *A&A*, **633**, A69
- Hildebrandt, H., van den Busch, J. L., Wright, A. H., et al. 2021, *A&A*, **647**, A124
- Hirata, C. M., & Seljak, U. 2004, *Phys. Rev. D*, **70**, 063526
- Hoffmann, K., Secco, L. F., Blazek, J., et al. 2022, *Phys. Rev. D*, **106**, 123510
- Hunter, J. D. 2007, *Comput. Sci. Eng.*, **9**, 90
- Jarvis, M., Bernstein, G., & Jain, B. 2004, *MNRAS*, **352**, 338
- Jing, Y. P. 2002, *MNRAS*, **335**, L89
- Joachimi, B., Mandelbaum, R., Abdalla, F. B., & Bridle, S. L. 2011, *A&A*, **527**, A26
- Joachimi, B., Semboloni, E., Hilbert, S., et al. 2013, *MNRAS*, **436**, 819
- Joachimi, B., Lin, C. A., Asgari, M., et al. 2021, *A&A*, **646**, A129
- Johnston, H., Georgiou, C., Joachimi, B., et al. 2019, *A&A*, **624**, A30
- Johnston, H., Wright, A. H., Joachimi, B., et al. 2021, *A&A*, **648**, A98
- Jones, E., Oliphant, T., Peterson, P., et al. 2001, *SciPy: Open source scientific tools for Python*
- Kiessling, A., Cacciato, M., Joachimi, B., et al. 2015, *Space Sci. Rev.*, **193**, 67
- Kirk, D., Brown, M. L., Hoekstra, H., et al. 2015, *Space Sci. Rev.*, **193**, 139
- Kirk, D., Omori, Y., Benoit-Lévy, A., et al. 2016, *MNRAS*, **459**, 21
- Krause, E., Eifler, T., & Blazek, J. 2016, *MNRAS*, **456**, 207
- Kuijken, K., Heymans, C., Dvornik, A., et al. 2019, *A&A*, **625**, A2
- Lee, J., & Pen, U.-L. 2002, *ApJ*, **567**, L111
- Lewis, A., Challinor, A., & Lasenby, A. 2000, *ApJ*, **538**, 473
- Li, H., Zhang, J., Liu, D., et al. 2021, *ApJ*, **908**, 93
- Lin, W., & Ishak, M. 2017, *Phys. Rev. D*, **96**, 083532
- Liu, J., & Hill, J. C. 2015, *Phys. Rev. D*, **92**, 063517
- Liu, X., Liu, D., Gao, Z., et al. 2021, *Phys. Rev. D*, **103**, 123504
- Mandelbaum, R. 2018, *ARA&A*, **56**, 393
- Mandelbaum, R., Hirata, C. M., Seljak, U., et al. 2005, *MNRAS*, **361**, 1287
- Mandelbaum, R., Hirata, C. M., Ishak, M., Seljak, U., & Brinkmann, J. 2006, *MNRAS*, **367**, 611
- Marques, G. A., Liu, J., Huffenberger, K. M., & Colin Hill, J. 2020, *ApJ*, **904**, 182
- Miller, L., Heymans, C., Kitching, T. D., et al. 2013, *MNRAS*, **429**, 2858
- Namikawa, T., Chinone, Y., Miyatake, H., et al. 2019, *ApJ*, **882**, 62
- Newman, J. A., & Gruen, D. 2022, *ARA&A*, **60**, 363
- Okumura, T., Jing, Y. P., & Li, C. 2009, *ApJ*, **694**, 214
- Omori, Y., Chown, R., Simard, G., et al. 2017, *ApJ*, **849**, 124
- Omori, Y., Baxter, E. J., Chang, C., et al. 2019, *Phys. Rev. D*, **100**, 043517
- Pedersen, E. M., Yao, J., Ishak, M., & Zhang, P. 2020, *ApJ*, **899**, L5
- Peng, H., Xu, H., Zhang, L., Chen, Z., & Yu, Y. 2022, *MNRAS*, **516**, 6210
- Planck Collaboration I. 2020, *A&A*, **641**, A1
- Planck Collaboration VI. 2020, *A&A*, **641**, A6
- Planck Collaboration VIII. 2020, *A&A*, **641**, A8
- Refregier, A. 2003, *ARA&A*, **41**, 645
- Rezaie, M., Seo, H.-J., Ross, A. J., & Bunescu, R. C. 2020, *MNRAS*, **495**, 1613
- Robertson, N. C., Alonso, D., Harnois-Déraps, J., et al. 2021, *A&A*, **649**, A146
- Rong, Y., Yi, S.-X., Zhang, S.-N., & Tu, H. 2015, *MNRAS*, **451**, 2536
- Samuroff, S., Blazek, J., Troxel, M. A., et al. 2019, *MNRAS*, **489**, 5453
- Samuroff, S., Mandelbaum, R., & Blazek, J. 2021, *MNRAS*, **508**, 637
- Schaan, E., Krause, E., Eifler, T., et al. 2017, *Phys. Rev. D*, **95**, 123512
- Secco, L. F., Samuroff, S., Krause, E., et al. 2022, *Phys. Rev. D*, **105**, 023515
- Shi, J., Kurita, T., Takada, M., et al. 2021, *J. Cosmol. Astropart. Phys.*, **2021**, 030
- Singh, S., & Mandelbaum, R. 2016, *MNRAS*, **457**, 2301
- Singh, S., Mandelbaum, R., & Brownstein, J. R. 2017a, *MNRAS*, **464**, 2120
- Singh, S., Mandelbaum, R., Seljak, U., Slosar, A., & Vazquez Gonzalez, J. 2017b, *MNRAS*, **471**, 3827
- Sun, Z., Yao, J., Dong, F., et al. 2022, *MNRAS*, **511**, 3548
- Tonegawa, M., & Okumura, T. 2022, *ApJ*, **924**, L3
- Troxel, M. A., & Ishak, M. 2012a, *MNRAS*, **419**, 1804
- Troxel, M. A., & Ishak, M. 2012b, *MNRAS*, **427**, 442
- Troxel, M. A., & Ishak, M. 2014, *Phys. Rev. D*, **89**, 063528
- Troxel, M. A., Krause, E., Chang, C., et al. 2018, *MNRAS*, **479**, 4998
- van den Busch, J. L., Hildebrandt, H., Wright, A. H., et al. 2020, *A&A*, **642**, A200
- van den Busch, J. L., Wright, A. H., Hildebrandt, H., et al. 2022, *A&A*, **664**, A170
- van der Walt, S., Colbert, S. C., & Varoquaux, G. 2011, *Comput. Sci. Eng.*, **13**, 22
- Xia, Q., Kang, X., Wang, P., et al. 2017, *ApJ*, **848**, 22
- Xu, H., Zhang, P., Peng, H., et al. 2023, *MNRAS*, **520**, 161
- Yang, X., Zhang, J., Yu, Y., & Zhang, P. 2017, *ApJ*, **845**, 174
- Yao, J., Ishak, M., Lin, W., & Troxel, M. 2017, *J. Cosmol. Astropart. Phys.*, **2017**, 056
- Yao, J., Ishak, M., Troxel, M. A., & LSST Dark Energy Science Collaboration 2019, *MNRAS*, **483**, 276
- Yao, J., Pedersen, E. M., Ishak, M., et al. 2020a, *MNRAS*, **495**, 3900
- Yao, J., Shan, H., Zhang, P., Kneib, J.-P., & Jullo, E. 2020b, *ApJ*, **904**, 135
- Yu, Y., Zhang, P., Lin, W., & Cui, W. 2015, *ApJ*, **803**, 46
- Yu, H., Zhang, P., Wang, J., Yao, J., & Wang, F.-Y. 2021, ArXiv eprints [arXiv:2106.03298]
- Zhang, P. 2010a, *MNRAS*, **406**, L95
- Zhang, P. 2010b, *ApJ*, **720**, 1090
- Zjupa, J., Schäfer, B. M., & Hahn, O. 2020, *MNRAS*, submitted [arXiv:2010.07951]
- Zonca, A., Singer, L., Lenz, D., et al. 2019, *J. Open Source Softw.*, **4**, 1298

Appendix A: Signal drop Q

We keep the main text of this paper focused on the physics and presenting the details of the SC method, more specifically the calculation for the lensing-drop Q^{Gg} and the IA-drop Q^{Ig} , in this appendix. The Q s are calculated through Eqs. 13 and 14, while the correlation functions being used are just the Hankel transform (similar to Eq. 4) of the angular power spectrum C^{Gg} and C^{Ig} . The associated C^{Gg} and $C^{\text{Gg}}|_{\text{S}}$ are calculated via:

$$C_{ii}^{\text{Gg}}(\ell) = \int_0^\infty \frac{q_i(\chi)n_i(\chi)}{\chi^2} b_{\text{g,eff}} P_\delta \left(k = \frac{\ell}{\chi}; \chi \right) d\chi, \quad (\text{A.1})$$

$$C_{ii}^{\text{Gg}}|_{\text{S}}(\ell) = \int_0^\infty \frac{q_i(\chi)n_i(\chi)}{\chi^2} b_{\text{g,eff}} P_\delta \left(k = \frac{\ell}{\chi}; \chi \right) \eta_i^{\text{Gg}}(z) d\chi. \quad (\text{A.2})$$

Similarly, the C^{Ig} and $C^{\text{Ig}}|_{\text{S}}$ are given by:

$$C_{ii}^{\text{Ig}}(\ell) = \int_0^\infty \frac{n_i(\chi)n_i(\chi)}{\chi^2} b_{\text{g,eff}} P_{\delta,\gamma'} \left(k = \frac{\ell}{\chi}; \chi \right) d\chi, \quad (\text{A.3})$$

$$C_{ii}^{\text{Ig}}|_{\text{S}}(\ell) = \int_0^\infty \frac{n_i(\chi)n_i(\chi)}{\chi^2} b_{\text{g,eff}} P_{\delta,\gamma'} \left(k = \frac{\ell}{\chi}; \chi \right) \eta_i^{\text{Ig}}(z) d\chi. \quad (\text{A.4})$$

Here, $\eta_i^{\text{Gg}}(z) = \eta_i^{\text{Gg}}(z_{\text{L}} = z_g = z)$ is the function that account for the effect of the SC selection Eq. 8 in the Limber integral, similarly for η_i^{Ig} . They are expressed as:

$$\eta_i^{\text{Gg}}(z_{\text{L}}, z_g) = \frac{2 \int dz_G^{\text{P}} \int dz_g^{\text{P}} \int_0^\infty dz_G W_L(z_{\text{L}}, z_G) S(z_G^{\text{P}}, z_g^{\text{P}}) K}{\int dz_G^{\text{P}} \int dz_g^{\text{P}} \int_0^\infty dz_G W_L(z_{\text{L}}, z_G) K}, \quad (\text{A.5})$$

$$\eta_i^{\text{Ig}}(z_{\text{L}}, z_g) = \frac{2 \int dz_G^{\text{P}} \int dz_g^{\text{P}} \int_0^\infty dz_G S(z_G^{\text{P}}, z_g^{\text{P}}) K}{\int dz_G^{\text{P}} \int dz_g^{\text{P}} \int_0^\infty dz_G K}, \quad (\text{A.6})$$

as in Yao et al. (2020b), where K is the galaxy-pair redshift distribution kernel:

$$K(z_G, z_g, z_G^{\text{P}}, z_g^{\text{P}}) = p(z_G|z_G^{\text{P}}) p(z_g|z_g^{\text{P}}) n_i^{\text{P}}(z_G^{\text{P}}) n_i^{\text{P}}(z_g^{\text{P}}), \quad (\text{A.7})$$

and S is the SC selection function:

$$S(z_G^{\text{P}}, z_g^{\text{P}}) = \begin{cases} 1 & \text{for } z_G^{\text{P}} < z_g^{\text{P}}, \\ 0 & \text{otherwise,} \end{cases} \quad (\text{A.8})$$

which correspond to Eq. 8 in the main text, and the lensing kernel is:

$$W_L(z_{\text{L}}, z_{\text{S}}) = \begin{cases} \frac{3}{2} \Omega_{\text{m}} \frac{H_0^2}{c^2} (1 + z_{\text{L}}) \chi_{\text{L}} (1 - \frac{\chi_{\text{L}}}{\chi_{\text{S}}}) & \text{for } z_{\text{L}} < z_{\text{S}} \\ 0 & \text{otherwise} \end{cases}. \quad (\text{A.9})$$

Here, z_x is the true- z where x can be ‘‘G’’ the source, ‘‘L’’ the lens, or ‘‘g’’ the galaxy number density. The galaxy photo- z distribution is $n^{\text{P}}(z^{\text{P}})$, and the redshift PDF (probability distribution function) is $p(z|z^{\text{P}})$.

As shown above, when the galaxy photo- z distribution and the corresponding true- z distribution are given, as shown in Fig. 3 in this work, we can follow the above procedure to calculate the lensing-drop Q^{Gg} and Q^{Ig} . The results of Q^{Gg} and Q^{Ig} for this work are shown in Fig. 4. Generally, given the tomographic bin width, the better photo- z is, the smaller Q^{Gg} will be (it reaches ~ 0 for perfect photo- z). On the other hand, non-

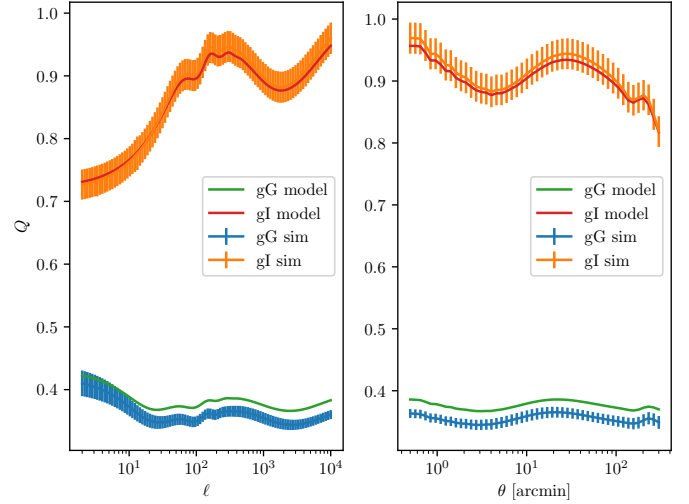


Fig. A.1. Effect of photo- z modeling with MICE2. By applying the SC selection in Eqs. 8 or A.8, the lensing-drop G^{Gg} from photo- z model (green) is slightly biased compared with the results from true- z (blue), while the IA-drop G^{Ig} from photo- z model (red) is immune to such bias and agrees with the true- z result (orange).

symmetric photo- z distribution and non-symmetric true- z distribution will make G^{Ig} deviate from 1. For more details on the Q calculation and its properties, we refer to the discussions in Yao et al. (2020a,b).

We note that for the SC calculation, the redshift PDF $p(z|z^{\text{P}})$ for each galaxy is required. Due to the fact that the PDFs from photo- z algorithm can be biased due to the color-redshift degeneracy in the photometric surveys, calibration is needed (Hildebrandt et al. 2017, 2021; Abbott et al. 2022). However, we can only statistically calibrate the overall redshift distribution $n(z)$ but not the PDF $p(z|z^{\text{P}})$ for each galaxy. This means in order to calculate Eq. A.7, we need to assume a photo- z PDF model. We chose to use a bi-Gaussian model Yao et al. (2020a)

$$p_{2\text{G}}(z|z^{\text{P}}) = (1 - f_{\text{out}}) p_{\text{main}}(z|z^{\text{P}}; \Delta_1, \sigma_1) + f_{\text{out}} p_{\text{outlier}}(z|z^{\text{P}}; \Delta_2, \sigma_2), \quad (\text{A.10})$$

with a main Gaussian peak and a Gaussian outlier peak with different bias, Δ_i , and scatter, σ_i , and an outlier rate, f_{out} .

We fit the bi-Gaussian model Eq. A.10, requiring it to have same mean redshift $\langle z \rangle$ with the SOM calibrated $n(z)$ (Asgari et al. 2021), and minimized the difference between the resulting model z -distribution $\int n^{\text{P}}(z^{\text{P}}) p(z|z^{\text{P}}) dz^{\text{P}}$ and the SOM $n(z)$. The best fit will then be a good description of the photo- z quality and can be used in Eq. A.7. The resulting signal drops are shown in Fig. 4 in the main text.

We validated the bi-Gaussian photo- z model for SC with MICE2 simulation. We made a comparison with the results that use the photo- z distribution and true- z distribution in the calculation of Eq. A.7. We show in Fig. A.1 that the bi-Gaussian model can produce the IA-drop Q^{Ig} measurement very consistently with those using true- z from simulations. However, we find the lensing-drop Q^{Gg} from the photo- z model is slightly higher than the true values from the simulation. This error will be propagated to the separated lensing signal w^{Gg} and the IA+magnification signal $w^{\text{Ig}} + g_{\text{mag}} w^{\text{Gk}}$, according to Eqs. (15) and (16). Its impact in A_{IA} is shown in Figs. 10 and 11.